Determination of Optimized Microwindows for Analysis of Absorption Spectra from Ground-based FTIR Spectrometer

by

Gizaw Mengistu

Thesis submitted to the School of Graduate Studies
of Addis Ababa University in partial fulfillment
of the requirement for the degree of
Master of Science
in
Physics

June, 1998
Addis Ababa

Acknowledgements

I would like to thank Drs. Thomas von Clarmann and Araya Asfaw for their advise and help with this work. I would also like to extend my gratitude to Dr. Georg Echle for his insight into this subject and constant help. Thanks also to Dr. Gabriele P. Stiller for her interest in the work and useful comments. Lastly, I would like to deeply thank German Academic Exchange Service for its financial support both during this work at Institute for Meteorology and Climatology, Forschungszentrum Karlsruhe, Germany and during my course work at Department of Physics, Addis Ababa University, Addis Ababa, Ethiopia.

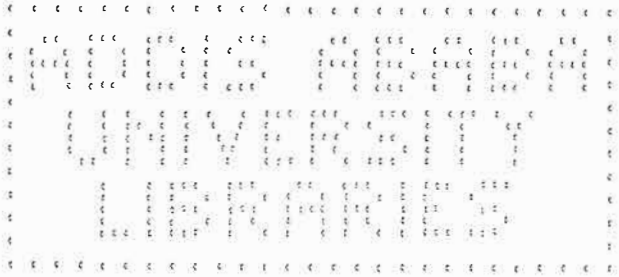

Contents

List of Tables

List of Figures

Abstract

In infrared remote sensing by Fourier transform spectroscopy usually not the measured spectrum as a whole is analysed but subsets, so-called "microwindows", which contain prominent transitions of the target species. While microwindows noted in the literature were selected by conventional methods, the purpose of this work is to select optimum microwindows for analysis of target species such that the related retrieval error is minimized. The choice of microwindows is shown to depend on the assumed retrieval scenario. In particular microwindow boundaries and associated retrieval errors are sensitive to assumptions on errors of parameters which are not jointly fitted along with the target parameters but kept constant during the retrieval. It is shown that consideration of uncertainities in pressure, temperature and measurement geometry has major influence on the optimization of microwindow boundaries and the selection of microwindows. Some of the microwindows which are optimum in the idealized case of negligible uncertainties of pressure, temperature and measurement geometry, are similar to those reported in the literature, while there are considerable differences between the latter and those microwindows optimized for more realistic conditions. Hence our analysis suggests that existing microwindows defined by conventional methods are not best suitable for application to realistic measurement scenarios because these sources of systematic errors have been underestimated.

1 Introduction

The principles of remote sensing are used for a wide variety of purposes, from examining the structure of the nucleus to the structure of stars, from oil exploration to medical tomography. The early development of remote sensing as a scientific field is closely tied to developments in photography. The first photographs were reportedly taken by Daguerre and Niepce in 1839. A number of progress have been made in the development of remote sensing since then. Beginning in the mid-1960's, a large number of studies of the application of color infrared and multispectral photography were undertaken under the sponsorship of NASA, leading to the launch of multispectral imagers on the Landsat satellites in the 1970's which were initiated due to two principal events. The first of these, during and after world war II, was the concerted military development of sensitive, fast-response detectors and compatible optical materials and later computers. The second, during late 1960's and early 1970's, was the emerging perception that manufactured chemicals in the atmosphere could affect the long-term stability of stratospheric ozone layer and the overall radiation balance of the planet. The concerns generated by this realization lead to development of instrumentation capable of first detecting, and then monitoring on a global scale, the concentrations of numerous source, sink, reactive and reservoir molecular species involved in these potential changes.

At the present time, most remote sounding investigations are directed towards the acquisition of fundamental information on composition, gross circulation, temperature and pressure patterns, and the nature and behavior of clouds. Recent concern has also been expressed that the steady build-up of source gases such as CO_2, CH_4, N_2O and CFC's affect the climate of the earth through change in the radiative transfer. Equally important is the possible depletion of the stratospheric ozone layer which plays a vital role in controlling the penetration of harmful UV radiation through the atmosphere. To this end, IR spectroscopy is of very great importance because the atmosphere absorbs and radiates strongly in this spectral region.

A brief historical development of remote sensing has so far been discussed mainly in relation to the development of instrumentation. In the following, the interpretation of

remotely sensed radiation measurements will be touched. Basically remote measurements are used when direct measurements are difficult or expensive since they often bring in their wake complex problems of interpretation generally known as Inverse Prohlems. The atmosphere is a typical subject for which remote measurements are cost effective, and for which inverse methods are required.

All remote sounding techniques involve the detection and measurement of electromagnetic energy after it has been emitted from, reflected from, partially absorhed by or otherwise modified by the part of the atmosphere of interest. The problem of interpretation of such measurements is made difficult by the fact that the flux intensity arriving at the instrument is, in general, a function of many unknowns, and made worse by the fact that the dependence is often complex and may be only partly understood.

The inverse problem is the question of finding the best representation of the required parameters given the measurements made, together with any appropriate a priori information that may be available about the system and the measuring device. Associated with the inverse problem there are also questions of understanding and describing the information content of the measurement, the relationship between the true state of the system and that derived using inverse methods, and the error analysis of the overall measuring system (Twomey, 1977).

The measured spectrum is usually not analysed simultaneously as a whole apparently due to much computer time involved. A single grid point is also impractical due to its limited information content. Hence, it is quite common to use a set of consecutive spectral grid points known as microwindow (e.g. Goldman et al., 1983, Gunson et al., 1990). The set of consecutive spectral grid points thus selected to extract information about the target species is expected to contain only small signal of interfering species. The analysis of the measured spectrum is usually carried out using inverse nonlinear modelling which is the basic approach of parameter fitting (Chang et al., 1977, Lin et al., 1979, Niple et al., 1980, Benner et al., 1995). The simulated spectrum is created on the basis of initial guess values of input parameters, and then compared to the measured one as a function of frequency grid points. The simulation with refined values of input parameters and comparison con-

tinues until there is a good agreement between simulated and measured spectra. For reasons of limited computational resources the analysis of measured spectrum as a whole is quite impracticable. Moreover, as the number of frequency grid points increases it is likely that more and more absorption features of other species of no interest but unknown abundances may increase as well. This in turn demands to increase the number of input parameters to describe the measured spectrum with more accuracy. In such situation, the nonlinear least squares refinement involves many parameters which sometimes may not lead to convergence.

The underlying reasons behind the conventional selection and definition of microwindows were purely ad hoc decisions of experienced spectroscopists in the early days of atmospheric spectroscopy. This does not promote the current demand for quantitative accuracy and measurement validation for reliable environmental monitoring and to our understanding of atmospheric chemistry and dynamics. Thus, selection and definition of microwindows have to be done quantitatively, objectively and in a reproducible manner.

An optimum microwindow contains prominent but usually non-saturated transitions of the target species, leading to high sensitivities of the measured spectral signal to the target parameters, while the signal of transitions of non-target species shall be low.

In this work, an attempt has been made to select optimum microwindows for spectral region 700.0 - 995.8 cm^{-1} for analysis of ground-based FTIR absorption spectra. We used formalism adopted from general theory of propagation of errors from several observables to less than or the same number of parameters. The results have been validated by doing some test retrievals for selected gases and then comparing associated retrieval errors with those claimed by the microwindows used.

2 Measurement of Absorption Spectra

2.1 The Instrument

The present study is dedicated to measurements of solar absorption spectra by ground-based high resolution FTIR spectrometers. An example of this type of instrument is the commercial BRUKER 120 HR spectrometer which is operated at several Network for Detection of Stratospheric Change (NDSC) stations to monitor the stratospheric composition. It is simply a technical variant of a common infrared spectrometer which yields an intensity signal as a function of wavelength. The setup differs from a classical grating or

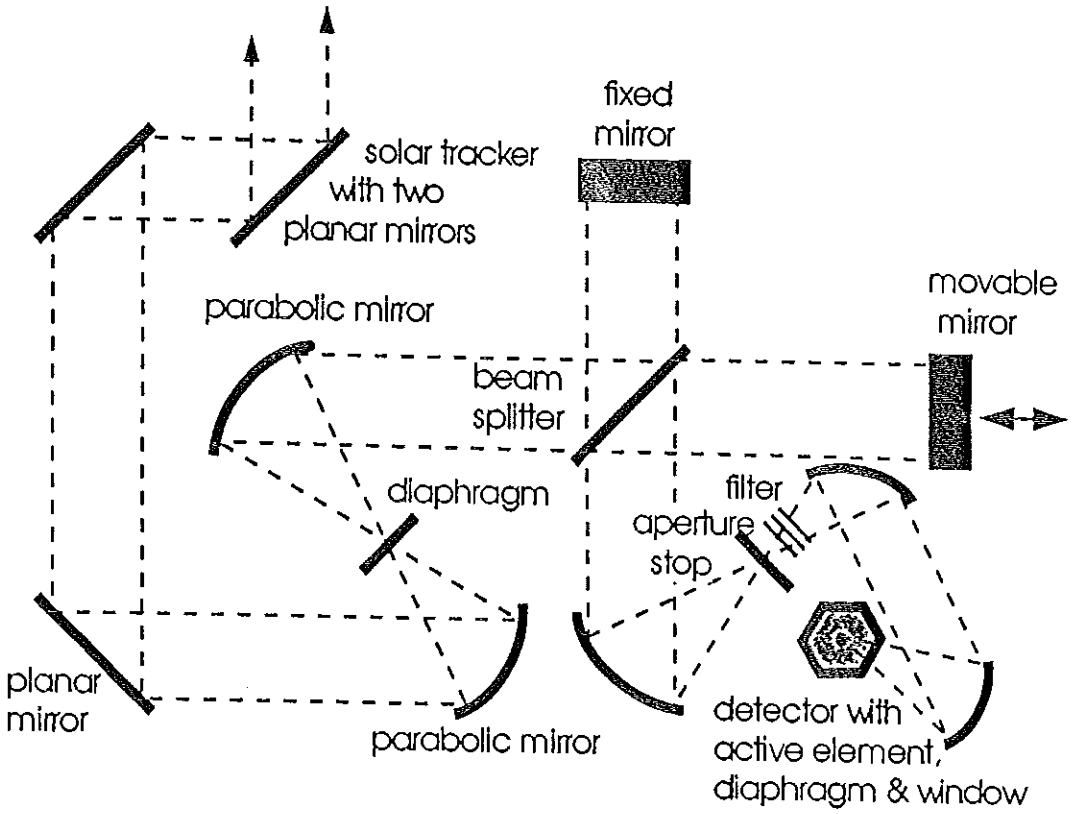

Figure 1: The schematic diagram of the FTIR Spectrometer.

prism spectrometer in that way, that it does not record the spectral intensity as a function of the wavelength directly but as an interferogram instead. The central component of an FTIR spectrometer is a Michelson interferometer. In such instruments amplitude division is usually performed through the use of a partially reflecting/transmitting surface called a beamsplitter. This generates two in-phase wave trains travelling in different directions. A

phase shift is introduced into one or both beams, and the two are recombined at another (or the same) partially reflecting surface.

The mirror system of the sun/moon tracker actively follows the position of the sun or moon, providing a homogeneous input of solar or lunar radiation into the actual spectrometer. The incident light is formed into a parallel beam by the pair of parabolic mirrors at the entrance of the instrument. The light then enters the Michelson interferometer consisting of the beamsplitter, the fixed and the movable mirrors, and the detector optics (see Fig. 1).

The detector considered in this particular study is a common Mercury-Cadmium-Tellurium (MCT) detector for solar spectra. The maximum optical path difference is 250 cm while the aperture of the interferometer and the focal length are 1.7 mm and 418 mm respectively. Therefore, the spectrometer has a resolution of 0.00255 cm^{-1} in terms of full width at half maximum (FWHM) after apodization with rectangular function.

2.2 Basic Implementation

Light from a point source (assumed monochromatic for the moment) is rendered parallel by a collimator (lens or mirror) . The wave front passes to a beamsplitter, here shown as an infinitely thin membrane (which in practice can be approximated) and is divided into two equal amplitude wave fronts. The two resultant wave fronts travel to the plane mirrors (assumed to be static for the moment) and are reflected back on themselves. Provided that the mirrors are set perfectly perpendicular to the beams, the wavefronts on recombination at the heamsplitter (now acting as a recombiner) are still plane and parallel and will interfere by the principle of superposition. After focusing by a condenser, a detector will record an intensity that depends on the path difference that was imposed by the travel to and from the plane mirrors.

The movable mirror in Fig. 1 was presumed to be a static system. Suppose, however, that it moves at a constant velocity of V [cm/s]. When illuminated by monochromatic point source, the detector will see a periodically varying signal and, it can be proved that the

output will be a cosine wave (Bell, 1972). The electrical frequency f [Hz] of this waveform is readily calculated: the rate of change of path difference $\frac{d\delta}{dt}$ is simply $2V$ [cm/s]; so we have

$$f = 2\nu V$$

remembering that the units of ν are cm^{-1}. That is, a Michelson Interferometer can be considered as a form of *frequency transducer* that converts optical frequencies (which are very high and well beyond the capability of the known detectors to sense) down to electrical frequencies that can, in principle, have any value we choose since the mirror velocity V is controllable by the user. Furthermore, the transformation is linear: the amplitude of the electrical output is directly proportional to the incoming intensity.

Suppose that we replace the monochromatic source by a broad band source. Such a source emits a wide range of optical frequencies that are independent (and uniquely) transformed into a range of electrical frequencies. The task now reduces to devising means of measuring the amplitudes of each of these electrical frequencies. If V is known, the input spectrum is immediately recoverable. In fact, a more elegant procedure is employed- the Fourier Transform (hence the name of the technique) (Bell, 1972, Beer, 1992).

2.2.1 The Basic Integral for Fourier Transform Spectroscopy

Here, we begin with the definition of Integral Fourier Transform and later show that the electric field as a function of position is the Fourier transform of the electric field as a function of frequency. Mathematically, a function $F(x)$ can be written as

$$F(x) = \int_{-\infty}^{\infty} A(\xi) e^{-i2\pi x\xi} d\xi \equiv \mathcal{F}^{-1}(A(\xi)).$$

If we know $F(x)$ and want $A(\xi)$, it is uniquely given by

$$A(\xi) = \int_{-\infty}^{\infty} F(x) e^{i2\pi\xi x} dx \equiv \mathcal{F}(F(x))$$

where this integral is called the Fourier transform and the earlier integral is called the Inverse Fourier transform.

Now consider a plane, monochromatic wave at a point z and at time zero. The wave may be represented by

$$y(z,\nu) = a(\nu)\cos(kz) = a(\nu)\cos(2\pi\nu z)$$

where k is the propagation constant and ν is the wave number. If at a point, one has many waves each of a different frequency and amplitude $a(\nu)$, then, in a wave train, the resultant amplitude is

$$y(z) = \frac{1}{\bar{\nu}}\int_0^\infty a(\nu)\cos(2\pi\nu z)d\nu. \tag{1}$$

Here, $\bar{\nu}$ is some average wave number and $\frac{a(\nu)}{\bar{\nu}}$ can be visualized as an amplitude density. The next step is to show that the amplitude limits can be extended from $-\infty$ to ∞, so that the Fourier transform integral can be used.

Consider the following separated integral:

$$\int_{-\infty}^{\infty} b(\nu)e^{i2\pi\nu z}d\nu = \int_{-\infty}^{0} b(\nu)e^{i2\pi\nu z}d\nu + \int_0^\infty b(\nu)e^{i2\pi\nu z}d\nu. \tag{2}$$

Note that, on reversing the limits of integration and using $b^*(\nu) = b(-\nu)$, one has

$$\int_{-\infty}^{0} b(\nu)e^{i2\pi\nu z}d\nu = \int_0^\infty b^*(\nu)(e^{i2\pi\nu z})^* d\nu. \tag{3}$$

Substituting (3) in (2) and noting that a complex product equals the complex conjugate of a product, one has

$$\begin{aligned}\int_{-\infty}^{\infty} b(\nu)e^{i2\pi\nu z}d\nu &= \int_0^\infty [b(\nu)e^{i2\pi\nu z} + (b(\nu)e^{i2\pi\nu z})^*]d\nu \\ &\equiv 2\int_0^\infty Re[b(\nu)e^{i2\pi\nu z}]d\nu. \end{aligned}\tag{4}$$

If $b(\nu)$ is real (it is also an even function), one has only the even part of the right integral, i.e., the cosine. Then, (4) can be arranged as

$$\int_0^\infty b(\nu)\cos(2\pi\nu z)d\nu = \frac{1}{2}\int_{-\infty}^{\infty} b(\nu)e^{i2\pi\nu z}d\nu. \tag{5}$$

Upon letting $b(\nu) = \frac{a(\nu)}{\bar{\nu}}$ and using (5), the resultant amplitude in (1) may be expressed as an integral from $-\infty$ to ∞ with the cosine function replaced by $e^{i2\pi\nu z}$ in the form

$$y(z) = \frac{1}{2}\int_{-\infty}^{\infty} b(\nu)e^{i2\pi\nu z}d\nu. \tag{6}$$

If we define $\frac{1}{2}b(\nu) = \mathcal{E}(\nu)$ as the electric field amplitude of wave number ν then the electric field as a function of position is the Fourier transform of the electric field given as a function of frequency

$$y(z) = \int_{-\infty}^{\infty} \mathcal{E}(\nu) e^{i2\pi\nu z} d\nu \equiv \mathcal{F}\{\mathcal{E}(\nu)\}. \tag{7}$$

A Fourier transform can be applied to (7), yielding

$$\mathcal{E}(\nu) = \int_{-\infty}^{\infty} y(z) e^{-i2\pi\nu z} dz. \tag{8}$$

We have so far derived the basic equation through which the electric field as a function of position, that can be obtained from direct measurement, is linked to the electric field as a function of frequency, that might be used to get the observed spectrum as briefly described in the next section.

2.2.2 A Spectrum Versus an Interferogram

An interferogram, the flux per unit solid angle, is a quantity that is measurable directly by the spectrometer as a function of the optical path difference of the interfering wave fronts (see Section 2.2). A spectrum is the same quantity but given as a function of its frequency. We demonstrate how one of these quantities is derived given the other.

The amplitudes of two coherent waves which at time zero have the same amplitude $\mathcal{E}(\nu)$ at wave number ν, but which are separated by a phase difference $k\delta = 2\pi\nu\delta$, can be given by (7) as

$$y_1(z) = \int_{-\infty}^{\infty} \mathcal{E}(\nu) e^{i2\pi\nu z} d\nu \tag{9}$$

and

$$y_2(z) = \int_{-\infty}^{\infty} \mathcal{E}(\nu) e^{i2\pi\nu(z-\delta)} d\nu \tag{10}$$

where δ is the optical path difference between the two waves. Eqns. (9) and (10) represent the waves from each arm of the interferometer after they have been recombined. Using the superposition principle, one has

$$y(z) = y_1(z) + y_2(z) = \int_{-\infty}^{\infty} [\mathcal{E}(\nu)(1 + e^{-i2\pi\nu\delta}) e^{i2\pi\nu z}] d\nu. \tag{11}$$

Define the resultant field $\mathcal{E}_R(\delta,\nu)$ as

$$y(z) \equiv \int_{-\infty}^{\infty} \mathcal{E}_R(\delta,\nu) e^{i2\pi\nu z} d\nu \tag{12}$$

and compare to (11) from which by uniqueness of Fourier transforms, we obtain

$$\mathcal{E}_R(\delta,\nu) = \mathcal{E}(\nu)(1 + e^{-i2\pi\nu\delta}). \tag{13}$$

But the intensity $F(\delta,\nu)$, usually referred to as irradiance or flux density, is

$$F(\delta,\nu) \equiv \frac{1}{2} c\epsilon_o \mathcal{E}_R{}^*(\delta,\nu)\mathcal{E}_R(\delta,\nu), \tag{14}$$

where ϵ_o is the electric permittivity of the free space and c is the velocity of light in vacuum. This can be further simplified to

$$F(\delta,\nu) = c\epsilon_o \mathcal{E}^2(\nu)[1 + \cos(2\pi\nu\delta)]. \tag{15}$$

There is no phase relation between the fluxes of different wave numbers at a given path difference δ from white light source. So, we add the fluxes of different frequencies and define $I_R(\delta)$ as

$$I_R(\delta) = \frac{1}{\bar{\nu}} \int_0^{\infty} F(\delta,\nu) d\nu.$$

Upon substitution the expression for $F(\delta,\nu)$ from (15) , this equation will have the form

$$[I_R(\delta) - \frac{1}{2} I_R(0)] = \sqrt{(\frac{2}{\pi})} \int_0^{\infty} [(\frac{c\epsilon_o}{\bar{\nu}})\mathcal{E}^2(\nu)\sqrt{(\frac{\pi}{2})}] \cos(2\pi\nu\delta) d\nu,$$

where at $\delta = 0$, $I_R(0) = \frac{2c\epsilon_o}{\bar{\nu}} \int_0^{\infty} \mathcal{E}^2(\nu) d\nu$. Writing the Fourier transform of this integral, we have

$$[(\frac{c\epsilon_o}{\bar{\nu}})\mathcal{E}^2(\nu)\sqrt{(\frac{\pi}{2})}] = \sqrt{(\frac{2}{\pi})} \int_0^{\infty} [I_R(\delta) - \frac{1}{2} I_R(0)] \cos(2\pi\nu\delta) d\delta.$$

The left-hand side of this equation by definition is the irradiance (see (14)), so that the final result obtained is

$$F(\nu) = (const) \int_0^{\infty} [I_R(\delta) - \frac{1}{2} I_R(0)] \cos(2\pi\nu\delta) d\delta. \tag{16}$$

This is the basic equation which relates the interferogram $(I_R(\delta) - \frac{1}{2} I_R(0))$, the measured flux density as a function of position, with the spectrum $F(\nu)$, the irradiance as a function of frequency, which is the finger print of the species emitting at the given wave number and also vital for deriving information about the parameters. In order to obtain the spectrum, it is only necessary to repeat the calculation of Fourier transform using (16) for

each wave number in the range of interest.

Unfortunately, we can not solve (16); at least not quite. First and foremost, the use of an integral sign implies that we have knowledge of δ at infinitesimally small intervals (i.e., an infinite number of samples). As we shall see soon, we can have (and only need) knowledge of δ at discrete intervals, which will entail replacing the integral by a summation but thereby rendering the problem tractable on a computer. Second, and equally important, the interferogram is produced by a real instrument and can be generated only over some finite range of path difference δ (0 to L, say). What are the implication of this ?

Knowing the measured output, called an interferogram ($I_R(\delta) - \frac{I_R(0)}{2} = G(\delta)$), only over a finite range is exactly equivalent to multiplying a theoretically infinite version of $G(\delta)$ by a function that takes the value 1 between $\delta = 0$ and $\delta = L$ and is 0 every where else. Such a function is usually called a boxcar function. Thus what we actually will try to solve is not (16) but a modified version

$$F'(\nu) = \int_{-\infty}^{\infty} G(\delta)B(\delta)\cos(2\pi\nu\delta)d\delta \tag{17}$$

where $B(\delta) = 1$ for $0 \leq \delta \leq L; 0$ otherwise. What we must now try to resolve is the relationship between $F(\nu)$, the answer we really want, and $F'(\nu)$, the answer we are actually going to get. The key lies in the procedure known as convolution. By convolution theorem if

$$c = h \otimes g$$

and $C(f), H(f)$ and $G(f)$ are the Fourier transforms of c, h and g then

$$C(f) = G(f)H(f).$$

The required relation between $F'(\nu)$ and $F(\nu)$ is therefore

$$F'(\nu) = F(\nu) \otimes J(\nu)$$

where $J(\nu)$ is the Fourier transform of the boxcar function $B(\delta)$. It can be easily demonstrated that, with appropriate normalization (for details see Bell, 1972),

$$\begin{aligned} J(\nu) &= \frac{\sin(2\pi\nu L)}{2\pi\nu L} \\ &= sinc(2\pi\nu L) \end{aligned} \tag{18}$$

in a shorthand notation.

2.3 Physical Interpretation

The impact of the sinc function on the "ideal" spectrum $F(\nu)$ is to smear out the fine structure. That is, any spectral structure significantly sharper than the sinc function will be lost. This is the definition of spectral resolution: the measure of the ability of the spectrometer to produce the incoming spectrum. Another way of looking at convolution is to imagine the sinc function as an averaging function. It is conventional to define the resolution as the full width at half maximum. Most importantly the resolution is seen to be inversely proportional to the maximum path difference.

A point not yet touched upon is the obvious fact that the sinc function shows negative peaks whose amplitudes dies out quite slowly. This turns out to be a problem only if certain not strictly legitimate operations are performed on the output spectrum. It is, however, possible to play numerical games with the interferogram that "dampout" the oscillations. The procedure is called apodization, but there is a price for any such procedure widens the central peak. Apodization always results in a loss of spectral resolution and can in addition, introduce some undesirable "cross talk" into the spectrum which is correlations between grid points. In the case of the Bruker 120 HR instrument the side wiggles of the sinc function cause only negligible oscillations in the spectrum.

2.4 Measuring Principle

The ground-based infrared spectrometer records spectra in the mid infrared by directly looking into the sun or the moon, which requires cloud free observation conditions. The homosphere or lower atmosphere from ground up to 100 km altitude contains more than 99 % of all atmospheric molecules. These molecules are overwhelmingly in their ground states, but have typically a fair number of unoccupied excited rotational and vibrational states that can be occupied by absorbing discrete energy amounts that are determined by their molecular specroscopic properties. These energies typically correspond to photon energies found in the infrared (Herzberg, 1945, Bauman, 1962). Thus, each molecular

species leaves a characteristic fingerprint of absorption lines in the solar spectrum recorded from ground, by which it can be detected and identified.

The energy taken up by the molecules is mostly transfered into heat, when returning to ground state. The strength of an absorption feature increases almost linearly over a wide range with the total number of molecules in the optical line of sight and is thus a measure for the total number of molecules. The analysis of the spectra is performed by comparing it to a computer simulated model atmosphere with absorption features calculated from spectroscopic data base such as HITRAN96 (Rothman et al., 1996). The results reported are total column amounts, which are the total number of molecules above the observer for a given species over an area of 1 cm^2 for Zenith geometry (integration over altitude across the atmosphere along an earth radial path) an example of which is found in Adrian et al., (1991, 1992).

3 Radiative Transfer Theory

3.1 Radiative Transfer Equation

Radiative transfer is a theory that permits the quantification of the signal received at the input to the remote sensor in terms of a parameter called radiance. At a given point in the media, the change in this parameter I_λ (given in units of W/(cm^2 st cm^{-1})) as a wave transverses a distance ds along the direction of propagation is given by

$$dI_\lambda = -k_\lambda \rho I_\lambda ds \tag{19}$$

where ρ is the density of the material [kg/cm^3], and k_λ represents the mass extinction cross section for radiation of wavelength λ (in units of cm^2/kg). Additional energy may arise due to thermal emission and multiple scattering from other directions at the same wavelength. This can be given by

$$dI_\lambda = \mathcal{J}_\lambda \rho ds \tag{20}$$

where $\mathcal{J}_\lambda$ is defined as the source function coefficent. Upon defining the source function $\mathcal{J}_\lambda$ as $J_\lambda = \frac{\mathcal{J}_\lambda}{k_\lambda}$ and combining Eqs. (19) and (20) give

$$\frac{dI_\lambda}{k_\lambda \rho ds} = -I_\lambda + J_\lambda. \tag{21}$$

For spherical and nonhomogeneous atmospheric layer, the optical path ds is related to the radial position vector in spherical coordinate system through the Snell's law of refraction. Consider the following model layers of the atmosphere with the $z-$ axis is in the upward direction. We also assume the atmosphere is homogeneous within the layers under consideration so that the optical path and the radial position vector coincides (no refraction) for the sake of simplicity and clarity. If θ is the zenith angle then a differential layer of the atmosphere along line of sight can be given as

$$ds = \frac{dz}{\cos(\theta)}.$$

Consequently, (21) has the form

$$\cos(\theta)\frac{dI(z,\theta,\phi)}{k\rho dz} = -I(z,\theta,\phi) + J(z,\theta,\phi). \tag{22}$$

It is quite common to refer to the medium elementary optical thickness along the vertical direction which is measured from the outer boundary downward and defined as

$$\tau_\lambda = \int_z^\infty k_\lambda \rho dz'.$$

Then we note that $d\tau = -k_\lambda \rho dz$ and (22) becomes

$$\mu \frac{dI}{d\tau}(\tau;\theta,\phi) = I(\tau;\mu,\phi) - J(\tau;\mu,\phi),$$

where μ =cos(θ). Suppose a radiation detector on the surface of the earth looks upward along the radial vector at a zenith angle θ . Then the incoming rays of the radiation will make angle of $\pi + \theta$. Hence, cos($\theta + \pi$) is negative leading to

$$-\mu \frac{dI}{d\tau}(\tau;-\mu,\phi) = I(\tau;-\mu,\phi) - J(\tau;-\mu,\phi). \tag{23}$$

Now multiplying both sides of (23) by $e^{-\frac{\tau}{\mu}}$ and integrating over τ gives

$$I(\tau;-\mu,\phi) = I(0;-\mu,\phi)e^{-\frac{\tau}{\mu}} + \int_0^\tau J(\tau';-\mu,o)e^{-\frac{(\tau-\tau')}{\mu}} \frac{d\tau'}{\mu},$$

where $I(0;-\mu,\phi)$ is inward source intensity at the top surface of the atmosphere. $J(0;-\mu,\phi)$ is the source function which depends on both scattering and thermal emission:

$$J(\tau';-\mu,o) = (1-\varpi)B(\nu,T(\tau')) + \frac{\varpi}{4\pi}\int_{4\pi} I(\nu,\tau',\omega')P(\nu,\omega,\omega')d\omega',$$

where $B(\nu,T(\tau'))$ is the Planck function at temperature $T(\tau')$ and ϖ is a single scattering albedo, the ratio of the scattering coefficient to the total extinction coefficient. More details on the topic can be found in Chandrasekhar (1960), Liou (1980), Goody and Young (1989), Lenoble (1985) and Kyle (1993). Measurements of absorption of solar (or other) radiation by atmospheric gases is described by the first term on the right hand side, where $I(0;-\mu,\phi)$ is the solar (or other) radiance at the top of the atmosphere. The instrument mentioned in Section 2.1 measures the absorption of solar (or lunar) radiation. Therefore, the appropriate term in the radiative transfer equation is the first term:

$$I(\tau;-\mu,\phi) = I(0;-\mu,\phi)e^{-\frac{\tau}{\mu}}. \tag{24}$$

In this case, $I(0;-\mu,o)$ is the Planck function of the source which for the case at hand refers to the sun. Upon dividing both sides of (24) by the Planck function gives the fraction of the solar radiation detected by the spectrometer after being attenuated by

atmospheric gases along the line of sight. Hence, one can also use transmission model equally well to describe the measurement. $e^{-\frac{\tau}{\mu}}$ is the total transmission between the points corresponding to optical paths $\tau = 0$, the top of the atmosphere, and $\tau = \tau$, at the site of the spectrometer. The radiative transfer model in terms of total transmission has the form

$$I(\mathcal{T}) = B(T_s)\mathcal{T}.$$

We then note that for attenuation of radiation between arbitrary atmospheric layers bounded by s_o and s:

$$I(\mathcal{T}) = B(T_s)\int_s^{s_o} \frac{\partial \mathcal{T}}{\partial s'} ds' \tag{25}$$

where now $\mathcal{T}$ is the total transmission after being attenuated by gases within layers bounded by s' and $s' + ds'$. This is a general model for which explicit functional form of $\mathcal{T}$ is not given, however, recalling the definition for optical thickness, the transmission can be expressed as a function of s:

$$\mathcal{T}(\nu, s) = exp\left[-\int_{s_o}^{s} \overline{k(\nu, s')}\rho(s')ds'\right]$$

with

$\rho(s) = \frac{p(s)}{k^B T(s)} =$ number density,

$p(s) =$ pressure,

$T(s) =$ temperature, and

$k^B =$ Boltzmann constant.

As there are many absorbers along the optical path, the absorption cross section is weighted and given by

$$\overline{k(\nu, s)} = \sum_{m=1}^{M} k_m(\nu, s)y_m(s)$$

where $y_m(s)$ and $k_m(\nu, s)$ stand, respectively, for volume mixing ratio (vmr) and absorption cross sections of the species m of the total number M of different molecular species that absorb in the spectral region under consideration. (24) can now be written as

$$I(\nu, s) = I(\nu, s_o)e^{-\int_{s_o}^{s}\sum_{m=1}^{M} k_m(\nu,s')y_m \frac{p(s')}{k^B T(s')} ds'}. \tag{26}$$

Furthermore, as the molecular species m may have several transitions which have different temperature and pressure dependence, the absorption cross section of one molecular species m as a function of temperature and pressure is given by the following sum over all lines of the species (see for more detail treatment e.g. Sparks (1997)):

$$k_m(\nu, T, p) = \sum_{l=1}^{lines} S_{m,l}(T) g_{m,l}(\nu - \nu_{m,l}, T, p) \tag{27}$$

where

$S_{m,l}(T) =$ line strength of line l of species m ;

$\nu_{m,l} =$ central wavenumber of line l of species m and

$g_{m,l} =$ line profile (line shape) .

The line strength is calculated using the formula

$$S_{m,l}(T) = S_{m,l}(T_o) \frac{Q_m(T_o)}{Q_m(T)} \frac{exp\left[-\frac{hcE''_{m,l}}{k^B T}\right]}{exp\left[\frac{hcE''_{m,l}}{k^B T_o}\right]} \frac{1 - exp\left[-\frac{hc\nu_{m,l}}{k^B T}\right]}{1 - exp\left[-\frac{hc\nu_{m,l}}{k^B T_o}\right]} \tag{28}$$

with

$S_{m,l}(T_o) =$ line strength at reference temperature T_o,

$Q_m =$ total internal partition function given at both reference temperature T_o and at temperature T,

$E''_{m,l} =$ lower state energy of the transition,

$h =$ Planck's constant and

$c =$ speed of light in vacuum.

For most of the conditions encountered in IR spectroscopy of the atmosphere, the actual line profile is the Voigt function which is the convolution of Lorentz and Doppler profiles and reduces to these functions in appropriate limits. It is given as:

$$g_{\nu,l} = \frac{1}{\alpha_D} \sqrt{\left(\frac{ln(2)}{\pi^3}\right)} a \int_{-\infty}^{\infty} \frac{e^{-t^2}}{a^2 + (x - t)^2} dt \tag{29}$$

where $a = \frac{\alpha_L}{\alpha_D}\sqrt{ln(2)}$; $x = (\frac{\nu-\nu_{m,l}}{\alpha_D})\sqrt{ln(2)}$.

The Doppler profile is given by

$$g^D_{m,l}(\nu - \nu_{m,l}, T) = \sqrt{\frac{ln2}{\pi}}\frac{1}{\alpha^D_{m,l}} exp\left[-ln2\frac{(\nu-\nu_{m,l})^2}{{\alpha^D_{m,l}}^2}\right]$$

with the half width at half maximum (HWHM) of the line $\alpha^D_{m,l} = \nu_{m,l}\sqrt{(2ln2\frac{K^B T}{M_m c^2}}$ where

M_m = molecular mass of species m.

The Lorentz function is

$$g^L_{m,l}(\nu - \nu_{m,l}, T, p) = \frac{1}{\pi}\frac{\alpha^L_{m,l}}{{\alpha^L_{m,l}}^2 + (\nu-\nu_{m,l})^2}$$

and the Lorentzian HWHM is

$$\alpha^L_{m,l} = \alpha^{L_o}_{m,l}\frac{p}{p_o}\left[\frac{T_o}{T}\right]^{\gamma_{m,l}}$$

with

$\alpha^{L_o}_{m,l}$ = Lorentzian half width at reference temperature T_o and pressure p_o,

$\gamma_{m,l}$ = coefficient of temperature dependence of the half width.

In general the integral with respect to s can not be solved analytically. The radiation path is usually broken up into homogeneous steps, i.e., where $k_m(\nu, s)$ and $\rho(s)$ are independent of s, and the integral is replaced by a sum thereby rendering the problem to be handled by numerical methods on computers.

Finally, having determined all the necessary parameters in (26) through Eqs. (27) - (29) and the line of sight (which is given by the viewing direction and the distribution of the refractive index in the atmosphere), the model evaluates the monochromatic radiance explicitly after being convolved with instrumental line shape (AILS, as given by (18)) to include the physical constraint of the spectrometer. Such a model is known as the "line-by-line" model. There are many codes developed for this type of model (e.g. Mankin, 1979, Edwards, 1987, Sparks, 1997) and we have used FASCOD2 (Clough, 1986).

In this particular studies the description of forward model of the radiative transfer is quite important since the spectra, that have been used to calculate the numeric Jacobian, and the synthetic spectra, that have been used as a measured spectra for test retrievals we require later in the sections to follow, are generated hased on this model.

3.2 The Retrieval Procedures

The theoretical model describes the system through a set of parameters so that the retrieval procedure consists of the search of the set of values of the parameters that produce the "best" simulation of the observations. The most commonly adopted criterion to accomplish the objective is the minimisation of the merit function (generally defined as the squared summation of the difference between observations and simulations) with respect to the value of the parameters. This criterion is generally known as least squares fit (LSF). When the forward model does not depend linearly on the unknown parameters then the problem of retrieval is that of non-linear least squares fit (NLSF), which can not be solved directly by using a solution formula, so that an iterative procedure must be used.

NLSF derives atmospheric parameters from iterative comparison of a measured spectrum with the related synthetic spectrum. Application of NLSF technique to high resolution spectra requires line-by-line spectral synthesis calculations. Given a set of N observed radiances $x_1, x_2, ..., x_N$ for which the above model is accurate, an estimate of the particular conditions that produced the spectrum can be obtained by matching it with a synthetic spectrum calculated using this model.

It is quite obvious that as the most practical convergence criterion is the simple one of a limit on the number of times a synthetic spectrum is calculated, each such calculation takes much of computer time and the situation being worse when one analyzes a large number of spectral grid points. To overcome such difficulty, there are several optimization schemes developed. We adopted the Levenberg-Marquardt method. Marquardt (1963) has developed an elegant method following an earlier suggestion of Levenberg (1944). Next, we show the basics of nonlinear least squares analysis followed by concepts

on which basis the Levenberg- Marquardt method is developed.

Any function f in a multidimensional coordinate system can be approximated by Taylor series

$$\begin{aligned} f(Y) &= f(Y_o) + \sum_i \frac{\partial f}{\partial y_i} y_i + \frac{1}{2} \sum_{i,j} \frac{\partial^2 f}{\partial y_i \partial y_j} y_i y_j + \ldots \\ &\simeq c - bY + \frac{1}{2} Y H Y \end{aligned} \tag{30}$$

where $c = f(Y_o)$, $b = - \bigtriangledown f|Y_o$ and $H_{i,j} = \frac{\partial^2 f}{\partial y_i \partial y_j}|Y_o$.

Following (30), the gradient of f is easily calculated as

$$\bigtriangledown f = HY - b$$

which yields

$$HY = b \tag{31}$$

at an extremum.

It is not uncommon to choose merit function that measures the agreement between the data and the model with a particular choice of parameters. Towards this end, we can define R to be such a merit function which is well approximated by (30) at sufficiently close to the minimum. Suppose y_0 is initial guess and y_{min} is the value at which merit function is minimum then

$$\bigtriangledown R(Y_o) = HY_o - b \tag{32}$$

and at minimum

$$HY_{min} = b \tag{33}$$

as given in (31). Upon subtracting (33) from (32) and multiplying by the inverse Hessian matrix H^{-1} gives

$$Y_{min} = Y_o + H^{-1}[- \bigtriangledown R(Y_o)]. \tag{34}$$

On the other hand, (30) might be a poor local approximation to the shape of the function at X_o. In that case, about all we can do is take step down the gradient, as in the steepest descent method (see, e.g. Press et al, 1990):

$$Y_{next} = Y_o - const \times \bigtriangledown R(Y_o) \tag{35}$$

where the *const* is small enough not to exhaust the downhill direction.

Up to now, we have approximated the merit function by quadratic and devised a means of approaching the minimum. Now, we are in a position to use either (34) or (35) in case (34) fails, however, we must be able to compute the gradient of R at any set of parameters Y. We also need the matrix H to use (34). Indeed, these tasks are much simpler as we know exactly the form of R since it is based on a model function that we ourselves have specified. Proceeding further, let y represent all the model parameters whose values for x_i are unknown, and let y' represent all the parameters whose values are known. The least squares estimates $\bar{y}$ for values of the unknown parameters corresponding to x_i are defined to be those values which minimize

$$R(y) = \sum_{i=1}^{N} [x_i - I(\nu_i, y'; y)]^2.$$

The gradient of R with respect to the parameters y, which will be zero at the R mininum, has components

$$\frac{\partial R}{\partial y_k} = -2 \sum_{i=1}^{N} [x_i - I(\nu_i, y'; y)] \frac{\partial I(\nu_i, y'; y)}{\partial y_k}, \quad k = 1, 2, ..., M.$$

Taking additional partial derivatives gives

$$\frac{\partial^2 R}{\partial y_k \partial y_l} = 2 \sum_{i=1}^{N} [\frac{\partial I(\nu_i, y'; y)}{\partial y_k} \frac{\partial I(\nu_i, y'; y)}{\partial y_l} - [x_i - I(\nu_i, y'; y)] \frac{\partial^2 I(\nu_i, y'; y)}{\partial y_k \partial y_l}]$$

It is convenient to remove the factors of 2 by defining

$$\beta_k = -\frac{1}{2} \frac{\partial R}{\partial y_k}$$

and

$$\alpha_{kl} = \frac{1}{2} \frac{\partial^2 R}{\partial y_k \partial y_l}.$$

Making $[\alpha] = \frac{1}{2} H$ in (34), in terms of which that equation can be written as the set of linear equations:

$$\sum_{l=1}^{M} \alpha_{kl} \delta y_l = \beta_k. \tag{36}$$

This set is solved for the increments δy_l that, are added to the current approximation, to give the next approximation. The steepest descent formula, translates to

$$\delta y_l = const \times \beta_l. \tag{37}$$

The second derivative of the basis function in the Hessian matrix is often ignored mainly due to the fact that the factor multiplying this derivative can be taken as the random measurement error of each point for a successful model which at end add up to zero because of equal chance of being positive or negative over all observations.

We have seen that in the search for global minimum, one can switch to and from the two methods depending on whether the quadratic approximation is a poor local approximation or not. The Levenberg-Marquardt method devises combined optimum use of the two extremes based on two elementary, but important, insights.

The line of reasoning followed was that the quantity R is nondimensional which is evident from its definition. Besides, β_k has the dimension of $\frac{1}{y_k}$, which may well be dimensional so that the constant of proportionality between β_k and δy_k must therefore have the dimension of ${y_k}^2$. As a result $\frac{1}{\alpha_{kk}}$, the reciprocal of the diagonal element of the Hessian matrix, is the only candidate to set the scale of the constant in (37). This leads to

$$\delta a_l = \frac{1}{\lambda \alpha_{ll}} \beta_l \tag{38}$$

where λ is introduced to take care of the size of the scale which can be set to any desired value to cut down the steps.

Marquardt's second insight is that Eqs. (38) and (36) can be combined if we define a new matrix α' by

$$\begin{aligned} \alpha'_{jj} &= \alpha_{jj}(1 + \lambda) \\ \alpha'_{jk} &= \alpha_{jk}(j \neq k) \end{aligned}$$

and then replace both Eqs. (36) and (38) by

$$\sum_{l=1}^{M} \alpha'_{kl} \delta a_l = \beta_k. \tag{39}$$

Then, (39) switches to (38) for very large λ as the new matrix αI is forced to be diagonally dominant and to (36) for λ approaching zero. Thus, the method enables to come to convergence in a few iterations upon setting up a suitable algorithm.

4 Microwindow Selection

4.1 General Theory of Error Assessement

The model developed for the forward radiative transfer has to be used for inferences of the parameters from radiance observations. This is done by fitting the data to the model until the solution is found to be nearly unique by adjusting the parameters since one can arrive at different results only because of different initial guesses.

However, there are important issues that go beyond the mere finding of the best-fit parameters. Data are generally not exact. They are subjected to measurement errors called noise. Thus, typical data never exactly fit the model that is being used, even when the model is correct. We also need to assess whether or not the model is appropriate. Most important of all, we need to know the accuracy with which parameters are determined by the observations. In other words, we would like to quantify the propagation of random measurement noise to the derived parameters which can be done by error analysis method. In this section, a brief description of general theory of error analysis is presented and then the next section will explain how it has been adopted to microwindow optimization.

The forward radiative transfer model (25) is a model that involves many observables (as far as the radiance value at different grid points is considered, see the next section) and parameters. Therefore, it is a multivariate problem that requires multivariate error analysis.

The concept of variance and covariance is the core of multivariate error analyis. The covariance in the context of error analyis is a measure of how much of the errors in two quantities are correlated.

Consider the full set of n parameters $y_1, y_2, ..., y_n$ that are overdetermined by the m observables $x_1, x_2, .., x_m$ i.e. $m > n$ for which the principle of least squares estimate will have to be used to obtain the least variance estimates of the parameters. The principle of least squares states that it is the weighted sum of the differences that must be minimized to

obtain the best estimates of the parameters. Both for the error analysis and for the least squares or other parameters fitting calculations, weight must be assigned in advance to the observables which should be inversely proportional to the variances. Thus, the appropriate weighting method is to divide each element in the sum by a number proportional to the variance of the observables from which it was calculated. Let w_{ii} be the weight corresponding to the observable x_i, then

$$w_{ii} = \frac{\sigma^2}{\sigma^2(x_i)},$$

where σ^2 is a constant: the variance of an observable of unit weight. The sum to be minimized in the least squares calculation is then

$$S = \sum_{i=1}^{m} \epsilon^2(x_i) w_{ii}$$

where, ϵ is given by

$$\epsilon(x_i) = x_i(observed) - x_i(calculated).$$

It is given in matrix notation by

$$S = E^T W E$$

where E is a column matrix of the differences:

$$E = \begin{pmatrix} \epsilon(x_1) \\ \epsilon(x_2) \\ \vdots \\ \epsilon(x_m) \end{pmatrix}$$

and W, the weight matrix for uncorrelated observables, which is given by

$$W = \sigma^2 \begin{pmatrix} \frac{1}{\sigma(x_1)^2} & 0 & 0 & \cdots \\ 0 & \frac{1}{\sigma(x_2)^2} & \cdots & \cdots \\ \vdots & \vdots & \ddots & \vdots \\ 0 & 0 & \cdots & \frac{1}{\sigma(x_m)^2} \end{pmatrix}.$$

Thus, for uncorrelated observables, the weight matrix is inversely proportional to the variance-covariance matrix, S_x, through (see, e.g. Clifford, 1973):

$$W = \sigma^2 {S_x}^{-1}$$

By extension, the weight matrix for correlated variables is defined also as the inverse of the variance-covariance matrix; and thus given by the same equation but this time $S_x{}^{-1}$ is no more diagonal matrix.

The equations for linear least squares are first obtained and then extended to nonlinear model. In former case, the observables depend linearly on the parameters as:

$$X(calculated) = AY.$$

If Y is column matrix of parameters which are the best estimates obtained using the principle of least squares, then

$$E = X - AY$$

which yields

$$S = (X - AY)^T W (X - AY).$$

For a minimum value of S, $\frac{\partial S}{\partial y_i}$ must be zero for all values of i:

$$\frac{\partial S}{\partial y_i} = (X - AY)^T W(-A_i) + (-A_i)^T W(X - AY) = 0 \quad (i = 1, 2, .., m)$$

where A_i is a column matrix which is the i^{th} column of A. This leads to

$$A^T W A Y = A^T W X \tag{40}$$

which is the normal equation in matrix form.

For situations where the dependence of X and Y is not linear, least squares refinement must be applied. The calculation starts from initial guesses of the parameters which will be designated by $\bar{Y}$. From these values the calculated observables, $\bar{X}$, are obtained. If we define δ matrices by

$$\delta X = X - \bar{X},$$

and

$$\delta Y = Y - \bar{Y}$$

where X are the measured values of the observables and Y are the best estimates of parameters. We now assume that δX and δY are small enough so that the relation between them is approximately linear and the linear least squares equation given by (40) can be used to find δY from δX. The elements of A will now be $\frac{\partial x_i}{\partial y_j}$. The equations for obtaining the refinements are as follows:

$$\delta Y = (A^T W A)^{-1} A^T W \delta X \tag{41}$$

where W is the weight matrix. Here, we can notice that this equation is identical to (39). As we will realize soon, this is the basic reason as to why both approaches should yield the same results in principle.

This is being the case for linear least square estimate of the parameters, we will use it to derive a general expression for the variance-covariance matrix of the parameters. We must imagine that the complete set of observations is made a very large number, N, times and that on the i^{th} occasion, parameters Y_i are obtained by some methods based on the principle of least squares. Then if $\bar{Y}$ are the mean values of the parameters obtained after the N observations and $\delta Y_i = Y_i - \bar{Y}$ then the variance-covariance matrix, S_y, of the parameters will be given by

$$S_y = \frac{1}{N} \sum_{i=1}^{N} \delta Y_i \delta Y_i{}^T \tag{42}$$

We make the usual assumption that δX_i and δY_i are linearly related over the range of the errors, in which case δY can be expressed by equations of the form of (41)

$$\delta Y_i = (A^T W A)^{-1} A^T W \delta X_i$$

Thus, from Eqs. (41) and (42) as well as from the fact that the matrices W and $(A^T W A)^{-1}$ are symmetric, S_y is given by

$$\begin{aligned} S_y &= \frac{1}{N} \sum_{i=1}^{N} (A^T W A)^{-1} A^T W \delta X_i \delta X_i{}^T W A (A^T W A)^{-1} \\ &= (A^T W A)^{-1} A^T W S_x W A (A^T W A)^{-1}. \end{aligned} \tag{43}$$

4.2 Adaptation to Microwindow Optimization

Spectra recorded with ground-based instruments as described in Section 2.1 are obtained at zenith angles less than 90°. Observations at such geometry provide much poorer ver-

tical resolution than can be obtained by recording a sequence of observations at zenith angles greater than 90° from an elevated instrument. In principle there are some effects that can be used to derive altitude information from ground-based spectra example of which is the pressure-broadening of the spectral lines. This effect is used for instance by Stiller et al. (1995) for the retrieval of tropospheric and stratospheric partitioning of HCL from ground-based MIPAS FTIR spectra; by Hoell et al. (1980) to deduce vertical profiles of NH_3 in the troposphere from infrared heterodyne measurement of a single NH_3 line at 927.323 cm^{-1}, by Rinsland et al. (1982) and Goldman et al. (1983) for analysis of ground-based Fourier transform solar spectra with NLSF method. However, there is only limitted success story as only the general shape of the vertical distribution (e.g., peaked, uniform, sloped) could be deduced from the observed features. Often, a number of realistic vertical distributions were found to fit the spectra almost equally well. For example Goldman et al. (1986) noted little sensitivity to the tropospheric HCl profile, even when HCl features in several different zenith angle scans were fitted simultaneously and this was also noted by Stiller et al. (1995) in their investigation of the retrieval of tropospheric and stratospheric partitioning of HCl from ground-based MIPAS FTIR spectra. These and other works in the field confirmed that a well defined quantity that can be retrieved even when the details of the vertical profile can not be determined is the total gas column amount. In light of this, the error analysis method we will be adopting for optimum microwindow selection is targeted in the retrieval error of total column amounts.

As noted earlier, a certain combination of consecutive spectral grid points forms a microwindow. From this follows that optimum microwindow is a spectral interval consisting of grid points selected by minimizing the retrieval error δy_i of target quantity y_i. In most cases, the absorption feature of the target gas is blended with that of other interfering species for which we may require simultaneous fitting for deriving information about the target gas. As a result, the retrieval problem is not only a target quantity retrieval problem but also that of quantities related to major interfering species. Clarmann and Echle (1997) argued along this line of concept that even in the case of one target parameter the number of formal fit parameters usually exceeds one.

Suppose, the total column amounts of the n major interfering gases are sought to be retrieved in the spectral interval represented by m grid points. Let these quantities are given by a column vector

$$Y = \begin{pmatrix} y_1 \\ y_2 \\ \vdots \\ y_i \\ \vdots \\ y_n \end{pmatrix}$$

of which y_i is the target quantity. The measurement from which information is to be derived is represented by radiance values at each grid points which form column vectors of measurement or measurement vectors as Rodgers (1997) calls it. Therefore, the covariance matrix of the measurement S_x has a dimension of $(m \times m)$. It is also obvious that the transformation matrix A in the case of linear model and assumed to comprise elements $\frac{\partial x_i}{\partial y_j}$ in the case of nonlinear model becomes a matrix of dimension $(m \times n)$ which is often referred to as Jacobian matrix. This formulation enables us to make use of (43) for the estimate of the random retrieval error for which the covariance matrix of the measurement S_x contains the squares of the noise equivalent spectral radiances (NESR) of each grid point as diagonal elements. The off-diagonal elements sometimes differ from zero, because in Fourier spectroscopy the signals at adjacent spectral grid points are correlated due to oversampling as well as apodization and non-ideal instrumental line shapes.

When the fit parameters are overdetermined there are two methods of obtaining their standard deviations: either by propagation from the errors in the observables as in our case since we assumed that the standard deviations and correlation coefficients of the observables are known in advance, or by calculation from the sum of the squares of the differences. The weight matrix used is then the inverse of the variance-covariance matrix and $\sigma^2 = 1$. The random retrieval error given by (43) will now be

$$S_y = (A^T A)^{-1} A^T S_x A (A^T A)^{-1}.$$

Moreover, the noise is assumed to be the same at each spectral grid point. From this follows that the problem of propagating errors becomes one of calculating the variance-

covariance matrix of the parameters from that of observations. The procedure used therefore, is first to set up the variance-covariance matrix of the observables, the diagonal elements being the variance of the observables which must be assigned values in advance of the calculation (from other consideration). The off-diagonal elements are the covariances which will be zero if, as in our case, both of the following conditions are satisfied: (a) apodization for smoothing and mathematical filtering of the interferograms has not been applied and (b) the sampling is at Nyquist frequency.

If in the general case AILS is the normalized instrumental line shape of the instrument in the spectral domain and NESR is the noise equivalent spectral radiance of the unapodized spectrum then the element $S_{i,j}$ of the measurement covariance matrix S_x can be determined by linear convolution of the instrumental line shapes:

$$S_{i,j} = NESR^2 * \sum_k AILS_k \times AILS_{k-abs(i-j)}.$$

However, since in our case the sampling interval and the resolution of the interferometer is chosen to be the same, there is no correlations due to convolution process. Hence, the elements of measurement covariance matrix S_x can be calculated as

$$S_{i,j} = \begin{cases} NESR^2 & \text{if i=j} \\ 0 & \text{otherwise.} \end{cases}$$

There might also be other model parameters which are kept constant during inversion; as a consequence of which there will be some systematic errors in the derived parameters that are in linear approximation directly proportional to the a priori uncertainities of the former. These are estimated as follows. The retrieval errors $\delta y_{i,j}$ of the fit parameter y_i due to the error source j can be linearly approximated by (41) as

$$\begin{pmatrix} \delta y_{1,j} \\ \vdots \\ \delta y_{n,j} \end{pmatrix} = (A^T A)^{-1} A^T (X_{error,j} - X_{true}) \qquad (44)$$

where X_{true} is a synthetic spectrum generated as a reference forward calculation, while $X_{error,j}$ is a spectrum generated by the same type of calculation but with the j^{th} input parameter perturbed by one standard deviation. In situation when the sensitivity to the changes in these parameters by one standard deviation is significantly low it is possible to

use a suitable increment in the parameters and then to rescale by the corresponding a priori uncertainities. Typical systematic errors to be handled by this formalism as suggested by Clarmann and Echle (1997) are errors due to temperature uncertainties in case of trace gas retrievals, errors due to inaccurate pointing of the instrument, errors due to wrong assumptions on abundances of species which contribute to the signal in the microwindow and which are not fit parameters but kept constant.

The systematic nature of these types of retrieval errors lead to the following covariance matrix, $S_{i,j}$, representing the retrieval errors due to error source j

$$S_{i,j} = \begin{pmatrix} {\delta y_{1,j}}^2 & \cdots & \delta y_{1,j}\delta y_{k,j} \\ \vdots & \ddots & \vdots \\ \delta y_{k,j}\delta y_{1,j} & \cdots & {\delta y_{k,j}}^2 \end{pmatrix}.$$

Now, representing the random errors in a priori information that are not correlated by $\delta y_{i,j}$, j running from one to the number j_{max} of uncorrelated systematic errors under consideration, the final estimated retrieval error δy_i of the target quantity y_i is calculated as

$$\delta y_i = \sqrt{{\sigma_i}^2 + \sum_{j=1}^{j_{max}} (\delta y_{i,j})^2}. \tag{45}$$

The retrieval error decreases when the microwindow becomes wider since more information on the target species is added. However, if the width exceeds some optimum value, the systematic errors as a result of inclusion of signal of interfering species having high a priori uncertainities may begin to increase. Thus, there has to be a trade off between different error sources. This can be done with suitable software which searchs for a combination of consecutive spectral grid points that yields the minimum possible retrieval error following the implementation given by the next section.

4.3 Computational Methodology

The procedure hereafter is to evalute a nominal spectrum X_o of dimension m for the spectral region under investigation along with increment spectra for all parameters whose effects are to be considered for the selection of the microwindows. The nominal spectrum is generated for model atmosphere consisting of 43 level values of pressure, temperature, and vmr of 17 target species from ground to an altitude of 70 km under local thermodynamic equilibrium (LTE) which were synthesised from radiosonde data and other independent methods for chemically unperturbed polar winter condition (Echle et al., 1992). Additional description of the type of profile used for individual gas is given in Section 5.1. Besides, the spectra for the 21 parameters X_j are calculated under the same

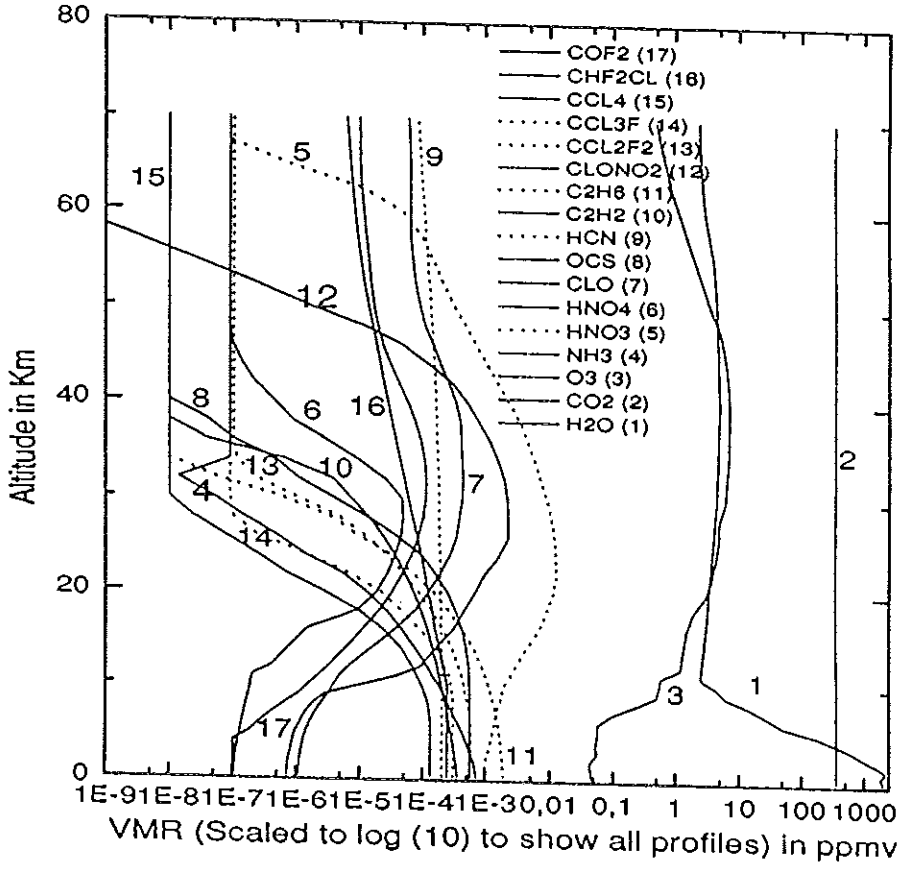

Figure 2: The volume mixing ratio of the target gases as a function of altitude.

ple, the Jacobian matrix must be evaluted at the best estimate profile obtained from the final cycle of the nonlinear least squares refinement procedure. However, this has been bypassed by assuming realistic profile which we often call it as reference profile. As a consequence, results obtained here refer to climatological conditions rather than individual

measurements. Having S_x, A, X_o, and X_j, the retrieval error can be estimated for each microwindow $[m_1, m_2] \epsilon [1, m]$, where m_1 and m_2 denote the boundary of the microwindow.

In order to avoid an underdetermined inversion problem, the minimum number of in-

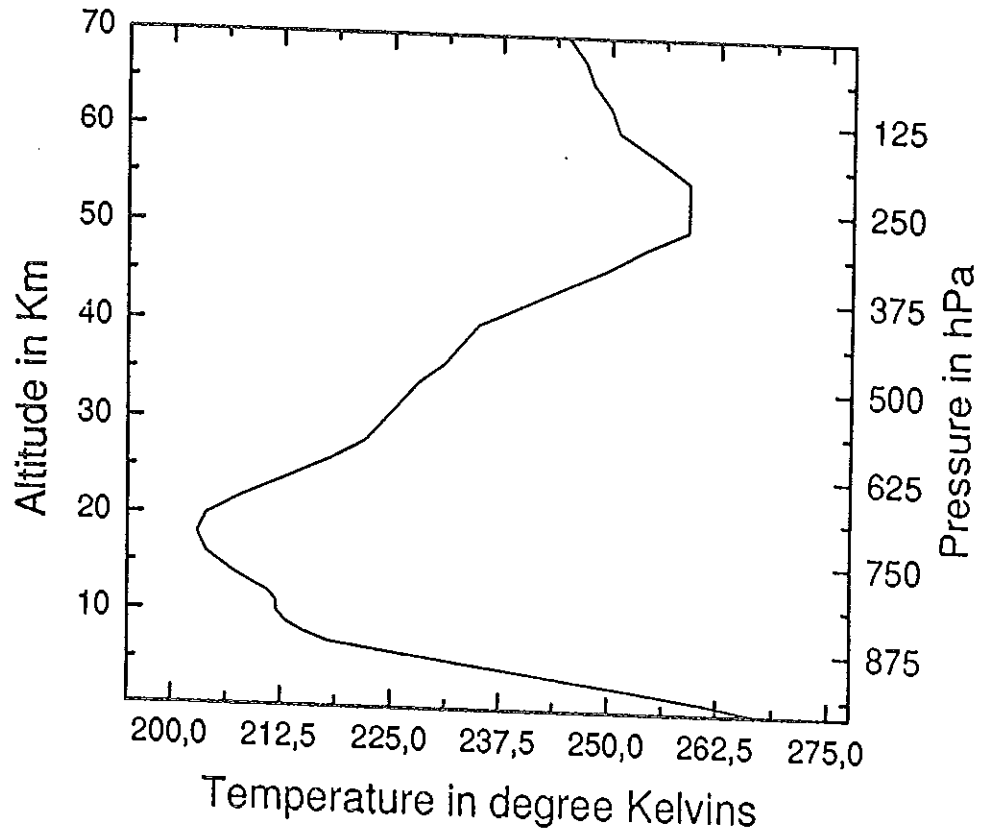

Figure 3: The Reference Temperature-Pressure profile used for the model atmosphere.

dependent grid points to start with must be equal to the number of fit parameters n as a result of which the first guess microwindow $[m_1, m_2]$ is set up as $m_1 = 1$ and $m_2 = n$. The total retrieval error of the target parameter is estimated by means of (45). Then, m_2 is increased until a local minimum of the retrieval error $\delta y_{i,min}$ is achieved. A further growth of m_2 would lead to an increased total error because the systematic portion of the error would begin to overcompensate the gain of information by inclusion of additional grid points.

A new guess microwindow is set up where the right microwindow boundary is related to the local minimum of the retrieval error. The current guess left boundary of the mi-

crowindow is initialized as $m_2 - n + 1$, and decreased in steps of one until the estimated retrieval error is minimized. Boundaries of the first microwindow having been determined, further microwindows are defined in a similar manner, starting one grid point apart from the right boundary of the first microwindow.

To prevent extensive splitting of microwindows which often arises due to a negligible transition of very low intensity of interfering species whose abundance is unknown, a

parameter	Standard deviation(%)	parameter	Standard deviation(%)
H_2O	10	HCN	25
CO_2	1	C_2H_2	10
O_3	5	C_2H_6	10
NH_3	15	COF_2	25
HNO_3	10	CCl_2F_2	20
$ClONO_2$	25	CCl_3F	20
HNO_4	50	CCl_4	20
ClO	50	CHF_2Cl	20
OCS	15		

Table 1: A priori uncertainty considered for each target species.

$\delta y_{i,min}$ is reached by increasing m_2, this value and corresponding value of m_2 is stored while continuing to increase the right boundary. If the immediate microwindow has total retrieval error which differs from the previous by more than ϵ then there will be no further increase of m_2 and thus the microwindow will be defined with the previous m_2 as a boarder. This means that the increase in the total retrieval error is due to non-negligible transition of interfering species and hence it must be taken into account. If the other option is satisfied then an increment in the error due to inclusion of one grid point may be accounted as allowance given to error fluctuation so that searching for the right boundary will proceed further until the current total error exceeds the previous by more than ϵ.

An a priori standard deviation of the column amounts considered for all the gases is indicated in Table 1. The standard deviation assumed is 1 % for pressure, 0.03 ° for

angle of observation, 2 ° Kelvin for both tropospheric and stratospheric temperatures while the increment for the forward model calculation is 0.1 ° for angle of observation, 0.5 % for pressure, 0.5° and 2 ° Kelvin for stratospheric and tropospheric temperatures in that order. The residual spectra should have been evaluated from nominal spectrum and increment spectra obtained at an increment of one standard deviation of the vmr for each species. But, this is not the case mainly due to the weak sensitivity of the absorption to an increment of one standard deviation for some species leading to singular Jacobian matrix. Therefore, the reference profiles are perturbed at increment of 10 % to simulate increment spectra and then the residual spectrum, $X_{error,j} - X_{true}$, in (44) is scaled to assumed uncertainity by:

$$X_{error,j} - X_{true} = \frac{X_{increment} - X_{reference}}{increment} * uncertainty.$$

The volume mixing ratios of the target species and temperature-pressure profile for the model atmosphere used in this work are given in Figs. 2 and 3.

5 Results and Validation

5.1 Results

We have investigated seventeen target species for which retrieval of column amount in the mid IR spectrum region (700.0-995.8 cm^{-1}) is assumed for two cases. We defined the first of these cases such that uncertainities in pressure and temperature (PT) as well as angle of sight (AOS) are taken into account in the microwindow optimization. This test case henceforth is referred to as PTAOS, and resulting microwindows are called PTAOS microwindows. For the second test case pressure, temperature and angle of sight have been assumed to be exactly known, and related retrieval errors therefore have been neglected during microwindow optimization. This test case is henceforth referred to as non-PTAOS, and resulting microwindows are called non-PTAOS microwindows.

The motivation to define two cases is mainly for the following reasons. The reason for PTAOS test case is entirely linked to the fact that the purpose of selection of optimized microwindows is to retrieve information from analysis of measured spectrum in this region about the target parameters with best possible precision by avoiding interference from other parameters known with very low accuracy. Hence, as many uncertain model parameters as possible have to be included in the selection of the microwindows in order to make results applicable to realistic scenarios. The reason for the second test case is mainly to compare the optimised microwindows with already existing ones. These latter ones were selected by experienced spectroscopists based on qualitative estimation of such effects as: interference by other absorbing gases in the spectral interval, temperature dependence of absorption lines of target species (but usually not the interfering ones) and accurate pointing of the instrument. In most cases, these spectral regions are assumed to be regions of less interference and weak temperature dependence (Toon et al., 1989, Brown et al., 1992 and references therein, Reisinger et al., 1995). As shown later, the non-PTAOS microwindows are better comparable to the microwindows defined by conventional methodology.

5.1.1 PTAOS Microwindows

PTAOS microwindows are microwindows optimized with respect to a priori uncertainities of pressure, temperature, angle of sight and minor interfering gases as well as the random retrieval error of target gas for which suitable microwindows are sought and its correlation with the retrieval errors of major interfering gases. Major interfering gases are gases whose interferences are such strong that they are jointly fitted along with the target parameter instead of being kept constant. Minor interfering species are species causing such weak interferences that their a priori uncertainities can be accepted. Abundances of these gases have been assumed to be constant during fitting process. These gases are considered as contributor to systematic portion of the error budget of the retrieval scenario.

Additional parameters such as zero level offset, background level and frequency shift are assumed to be known exactly. These parameters appear neither as joint fit parameters nor as source of systematic error. Furthermore, spectroscopic data were assumed to be perfectly known for both target and interfering species. i.e. uncertainities of these quantities are not considered for the microwindow selection.

Before defining a scenario, identification of major and minor interfering species with the signal of the target gas is made from preliminary analysis of residual spectra obtained from nominal and increment spectra. As described in the last section, the increment spectra are generated after perturbining the reference profile by 10 % of vmr of the target gas for all species investigated.

Following the selection, we have checked the presence and the number of transition lines and their corresponding line parameters within and in the neighbourhood of ± 0.05 cm^{-1} of the right and left boundaries of microwindow respectively. In all the cases with the exception of where explicit reference is made, there are quite a large number of transition lines and the list of strong absorption line along with its parameters are included (see Table 3).

The profiles used for simulation are all discussed in detail in a final report on measurements of atmospheric parameters with MIPAS by Echle et al., (1992). With this understand-

ing, from now onwards we will only mention the profiles used and changes made (if any) without further mention of the sources. While only the best microwindows are discussed in the following, a more complete list is found in the Appendix.

Acetylene (C_2H_2)

Acetylene is grouped as light hydrocarbons. Its source is purely at the earth's surface but due to its long life time in the troposphere, it is found to reach the stratosphere by atmospheric dynamics. Model calculations and measurements of C_2H_2 provide a wide range of vmr (Echle et al., 1992 and references therein). We took the mean of maximum and minimum profiles to represent C_2H_2 profile under the normal polar winter model atmosphere.

The preliminary investigation of the difference spectrum for C_2H_2 as the target gas revealed that H_2O, CO_2 and O_3 are the major interfering gases where as C_2H_6, CHF_2Cl, HNO_3, CCl_4, HCN, COF_2, and $ClONO_2$ are the species having relatively weak signal in the regions of strong C_2H_2 transitions. There are several microwindows of which we have reported only the first best 10 microwindows.

The first best two microwindows found do not include the spectral region which have been considered suitable and used by most investigators (Meier et al., 1997). The first microwindow has two absorption lines which have temperature dependence (E"=359 cm^{-1} and 1090 cm^{-1}) compared to microwindows (e.g 766.350-767.175 cm^{-1}, reported by Meier et al., (1997)) having the strongest absorption line whose temperature dependence is E"=282 cm^{-1}. We feel that there is no physical reason to expect similarity of the two results as the selections were made entirely on different basis; however, such question like why the first microwindow does not contain the strong absorption and weak temperature dependent line of C_2H_2 such as E"=282 cm^{-1} (see Table 3) may be raised. The answer lies in the fact that the major interfering species like CO_2 have relatively strong absorption lines in the microwindow containing this line which are highly sensitive to temperature change as compared to the best microwindow containing relatively weaker lines of C_2H_2 (Rothman et al., 1996).

Spectral interval cm^{-1}	Target gas	Major interfering species (Fit parameters)	Minor interfering species (Fixed parameters)
700.0-830.0	CO_2	H_2O	HNO_3, NH_3, C_2H_2, CHF_2Cl, CCl_4, HCN, $ClONO_2$, COF_2, ClO, HNO_4, O_3, C_2H_6,
920.0-995.8	CO_2	H_2O	NH_3, CCl_2F_2, O_3, COF_2
858.5-887.0	NH_3	H_2O, HNO_3, OCS, CCl_2F_2	C_2H_2, C_2H_6, CHF_2Cl, HCN, $ClONO_2$, COF_2, CCl_4, ClO
885.5-920.0	NH_3	H_2O, HNO_3, CCl_2F_2	C_2H_2, C_2H_6, CHF_2Cl, HCN, $ClONO_2$, COF_2, CCl_4, ClO
918.5-930.0	NH_3	H_2O, HNO_3, CO_2	C_2H_2, C_2H_6, CHF_2Cl, HCN, $ClONO_2$, COF_2, CCl_4, ClO
928.5-970.0	NH_3	H_2O, CO_2	C_2H_2, C_2H_6, CHF_2Cl, HCN, $ClONO_2$, COF_2, CCl_4, ClO
968.5-995.8	NH_3	H_2O, O_3, CO_2	C_2H_2, C_2H_6, CHF_2Cl, HCN, $ClONO_2$, COF_2, CCl_4, ClO
858.5-870.0	HNO_3	CO_2, H_2O, OCS	C_2H_6, NH_3
887.5-920.0	HNO_3	H_2O, CCl_2F_2	C_2H_6, NH_3
750.0-820.0	$ClONO_2$	H_2O, O_3, CO_2	C_2H_2, C_2H_6, CHF_2Cl, HCN, NH_3, COF_2, ClO, CCl_4, HNO_3, HNO_4
838.5-860.0	OCS	H_2O, HNO_3, CCl_3F	NH_3, C_2H_6, ClO, CHF_2Cl
858.5-889.0	OCS	H_2O, HNO_3, CCl_2F_2	NH_3, C_2H_6, ClO, CHF_2Cl

Table 2: A list of scenarios under which the reported optimized microwindows are found.

Spectral interval cm^{-1}	Target gas	Major interfering species (Fit parameters)	Minor interfering species (Fixed parameters)
710.0-800.0	HCN	H_2O, O_3, CO_2	C_2H_2, C_2H_6, CHF_2Cl, COF_2, NH_3, CCl_4, HNO_3
705.0-800.0	C_2H_2	H_2O, O_3, CO_2	C_2H_6,CHF_2Cl, CCl_4, HNO_3, $ClONO_2$, COF_2, HCN
770.0-831.0	C_2H_6	CO_2	H_2O, HNO_3, NH_3, CCl_3F, CCl_2F_2, C_2H_2, OCS, CCl_4, CHF_2Cl, HNO_4, COF_2, $ClONO_2$, HCN, ClO
829.0-860.0	C_2H_6	OCS, CCl_3F	H_2O, HNO_3, NH_3, CCl_2F_2, C_2H_2, CHF_2Cl, CCl_4, CO_2, HCN HNO_4, COF_2, $ClONO_2$, ClO
785.0-807.0	CCl_4	H_2O, CO_2, NH_3	O_3, C_2H_6, HNO_3, HCN, HNO_4, COF_2, C_2H_2,CHF_2Cl, $ClONO_2$
830.0-860.0	CCl_3F	H_2O, HNO_3, OCS	NH_3, C_2H_6,CHF_2Cl, ClO
888.5-937.0	CCl_2F_2	H_2O,HNO_3	NH_3, CO_2, C_2H_6, COF_2, ClO
780.0-830.0	CHF_2Cl	H_2O, CO_2	C_2H_6, NH_3, C_2H_2, CCl_4, HCN, $ClONO_2$, ClO, COF_2, HNO_4
818.5-850.0	ClO	H_2O, OCS	C_2H_6, NH_3, CHF_2Cl, $ClONO_2$, CCl_3F
848.5-885.0	ClO	H_2O, OCS	C_2H_6, NH_3, CCl_2F_2, HNO_3, CCl_3F
935.0-960.0	COF_2	H_2O, CO_2	NH_3
800.0-805.0	HNO_4	H_2O, CO_2, CCl_4, CHF_2Cl	NH_3, C_2H_6, ClO, $ClONO_2$,COF_2

Table 2 (continued).

Chemical species	Microwindow cm^{-1}	Strongest Absorption line	Intensity cm/molec.	E" in cm^{-1}	γ_{air} in cm^{-1}/atm	α of γ_{air}	Retrieval Error in %
C_2H_2	771.2853-771.6015	771.405	3.33E-19	359	0.0698	0.75	2.94
C_2H_2	759.3538-759.7287	759.695	1.89E-19	183	0.0803	0.75	4.23
C_2H_2	766.4224-766.7412	766.724	4.31E-19	282	0.0724	0.75	4.39
C_2H_2	761.5494-762.0517	762.039	5.27E-19	214	0.0798	0.75	4.70
C_2H_2	763.9770-764.5125	764.382	1.60E-19	247	0.0761	0.75	5.24
C_2H_2	775.8345-776.0997	776.081	2.43E-19	446	0.0702	0.75	6.09
C_2H_2	754.9041-755.1999	755.005	2.10E-19	129	0.0814	0.75	8.34
C_2H_2	780.5316-780.7662	780.752	1.67E-19	543	0.0649	0.75	8.80
C_2H_2	785.2236-785.6163	785.418	1.09E-19	649	0.0609	0.75	9.83
C_2H_2	766.7437-767.0089	766.805	1.40E-20	1012	0.0724	0.75	10.57
C_2H_6	819.2380-819.7301	819.549	2.01E-21	244	0.1000	0.50	7.58
C_2H_6	815.8082-816.9608	816.905	1.98E-21	292	0.1000	0.50	10.54
C_2H_6	822.3337-822.4178	822.343	2.25E-21	50	0.1000	0.50	14.30
C_2H_6	838.2636-838.7098	838.269	2.10E-21	58	0.1000	0.50	12.91
C_2H_6	830.2591-830.3866	830.275	1.75E-21	136	0.1000	0.50	13.92
HCN	747.3356-747.6085	747.405	1.56E-19	195	0.1053	0.50	30.94
HCN	762.0211-762.6085	762.121	8.07E-20	401	0.1044	0.50	33.65
HCN	750.0565-750.5231	750.351	1.42E-19	230	0.1062	0.50	33.96
HCN	753.1497-753.3741	753.295	1.27E-19	268	0.1044	0.50	39.29
HCN	758.9891-759.2263	759.180	9.54E-20	354	0.1035	0.50	41.18
OCS	842.5476-844.5340	844.499	1.14E-20	241	0.0885	0.72	9.34
OCS	855.6262-857.4752	855.687	8.17E-21	14	0.0990	0.77	9.91
OCS	848.0530-848.9557	848.898	1.44E-20	121	0.0925	0.70	10.33
OCS	845.6560-846.5562	846.273	1.44E-20	188	0.0900	0.70	10.84
OCS	844.5366-845.6381	845.389	1.22E-20	214	0.0890	0.71	10.91
OCS	849.9732-850.4321	850.194	1.45E-20	93	0.0940	0.71	12.42
OCS	770.1028-870.7352	870.201	1.45E-20	164	0.0905	0.70	9.52
OCS	868.3688-868.9477	868.713	1.54E-20	121	0.0920	0.70	10.66
OCS	866.6986-867.1499	866.826	1.53E-20	77	0.0945	0.71	11.81
OCS	868.9502-869.2767	869.087	1.53E-20	131	0.0915	0.70	12.16
ClO	860.7520-860.9127	860.832	3.24E-21	118	0.0930	0.75	139.20
ClO	831.3199-831.9651	-830.608	2.43E-21	72	0.0930	0.75	174.90

Table 3: A list of PTAOS microwindows found and the line parameters of the strongest absorption line in the microwindow for the gases indicated.

Ethane (C_2H_6)

Ethane is another light hydrocarbon for which the mean profile as described above is taken from the same source. The spectral regions with C_2H_6 signature have different interfering species which have no signal uniformly all over the spectral interval. This demands categorizing the whole spectral region into three subintervals and accordingly definition of three scenarios.

The region 770-831 cm^{-1} in which CO_2 is taken as a simultaneous fit parameter and

Chemical species	Microwindow cm^{-1}	Retrieval Error in %	Chemical species	Microwindow cm^{-1}	Retrieval Error in %
CCl_4	796.1988-796.8005	12.10	CCl_3F	850.0089-850.4321	3.89
CCl_4	794.2251-795.3343	13.70	CCl_2F_2	919.5779-919.9018	1.73
CCl_4	797.5987-798.0960	24.60	CCl_2F_2	922.9720-923.2627	1.88
CCl_4	789.7830-790.4868	25.18	CCl_2F_2	919.9044-920.6796	1.91
$ClONO_2$	780.0317-780.2306	8.97	CCl_2F_2	929.3853-929.6071	2.30
$ClONO_2$	780.2332-780.3734	13.02	CCl_2F_2	920.9346-921.1947	2.45
$ClONO_2$	806.8195-807.5820	16.80	CHF_2Cl	828.8949-829.5502	1.66
CCl_3F	843.1672-844.7329	2.31	CHF_2Cl	820.6456-820.9592	3.75
CCl_3F	848.1372-848.9328	2.96	CHF_2Cl	809.2114-809.3568	3.84
CCl_3F	842.2492-843.1647	3.49	CHF_2Cl	808.7703-809.2088	4.43
CCl_3F	850.4475-850.7254	3.72	CHF_2Cl	804.3026-804.5729	4.49

Table 4: A list of PTAOS microwindows found for gases with absorption cross sections.

the 829-860 cm^{-1} spectral interval with OCS and CCl_3F as major absorbers are the two spectral regions in which a significant number of good microwindows are found. We report five microwindows of which two are from the first spectral interval. The minor interfering gases considered for selection of microwindows from 770-831 cm^{-1} interval are H_2O, NH_3, HNO_3, OCS, CCl_3F, CCl_2F_2, C_2H_2, CHF_2Cl, CCl_4, HCN, $ClONO_2$, COF_2, ClO and HNO_4. H_2O, HNO_3, NH_3, CCl_2F_2, CO_2, C_2H_2, CHF_2Cl, CCl_4, HCN, $ClONO_2$, COF_2, ClO and HNO_4 are gases considered as weak absorber in the interval 829-860 cm^{-1}. Most of absorption lines of target gas that fall in the first best microwindow are having relatively weak temperature dependence compared to those in the second and other successive spectral intervals besides being of strong intensity (Rothman et al., 1996). A comparison of the first two microwindows from the first spectral interval mentioned above (see Table 3) in terms of the absorption lines of CO_2 showed that there are more CO_2 lines in

the second microwindow apart from strong temperature dependence.

Carbon Tetrachloride (CCl_4)

It belongs to family of halocarbons and is an anthropogenic source gas with a very long photochemical life time. Like any other halocarbons it is transported into the stratosphere where it is photochemically decomposed to provide free chlorine which takes part in catalytic destruction of ozone. Polar profile is taken for the simulation.

There are several microwindows having retrieval errors within tolerable limits. Major interfering species are H_2O, NH_3 and CO_2. The minor interfering absorbers are O_3, C_2H_6, HNO_3, C_2H_2, CHF_2Cl, HCN, COF_2, $ClONO_2$ and HNO_4. The first of these microwindows has no absorption lines of NH_3 and has comparatively weaker lines of CO_2 as compared to others.

Chlorine Monoxide (ClO)

ClO exhibits only rather weak absorption band in the mid-IR. It is a key radical involved in the catalytic destruction of atmospheric ozone and has been observed using FIR microwave and in situ techniques. The polar winter profile is used. There are three scenarios prepared for different spectral regions. Most of the microwindows found have retrieval errors of the order of several hundreds percent and two of these with relatively smaller retrieval errors are reported. This is partly attributed to low concentration of ClO in the atmosphere during normal polar winter. Therefore, the retrieval error is expected to reduce significantly under ozone hole condition during which very high concentration of this gas is observed.

Chlorine Nitrate ($ClONO_2$)

It is predicted to be a major temporary reservoir of chlorine in the middle stratosphere. It is formed by recombination of ClO with NO_2 and partly removed in the daytime by photolysis. The polar winter profile has been used after shifting maximum to 27 km and increasing the whole profile by a factor of 2 because of weak sensitivity. This change of the standard polar winter profile is justified by the high $ClONO_2$ mixing ratios observed by MIPAS-B (Clarmann et al., 1993). Several microwindows have been found with an error less than 50 % for the first scenario in the spectral region 750-820 cm^{-1} which includes

H_2O, CO_2 and O_3 as major spcecies and others (namely NH_3, C_2H_6, ClO, HCN, COF_2, CCl_4, HNO_4, CHF_2Cl and HNO_3) as minor. All the reported ones are found from this spectral interval. The spectral region 820-840 cm^{-1} where there are some transitions of $ClONO_2$ has only inferior microwindows as the associated error exceeds 50 % for all and report has not been made.

Carbon Dioxide (CO_2)

CO_2 is well mixed in the whole atmosphere up to the lower thermosphere and is a main component in the climate system. It is used for deriving the temperature distribution in the middle atmosphere due to its well known mixing ratio and strong absorption bands. The mean profile of 1991 is used after a trend correction by 10 ppmv in all the layers to account for the annual increase of concentration.

There are quite a large number of microwindows for CO_2 with only less than 10 % retrieval error derived from a scenario defined over spectral interval 700-830 cm^{-1}. As shown in Table 2, H_2O is the only species considered as major interfering and HNO_3, NH_3, O_3, C_2H_6, C_2H_2, CHF_2Cl, CCl_4, HCN, $ClONO_2$, COF_2, HNO_4 and ClO are minor interfering gases.

There are also similar number of microwindows from the second group over the spectral interval 920-995.8 cm^{-1} in which H_2O is major interfering gas and NH_3, O_3, CCl_2F_2 and COF_2 are weak absorbers. Report of four and six microwindows have been made, respectively, from the two retrieval scenarios.

Carbonyl Fluoride (COF_2)

It is an intermediate product in the decomposition of halocarbons in the stratosphere. Its importance lies in the need to understand the reactions that follow the break up of halocarbons in the stratosphere. The profile used is the mean profile.

Most of the microwindows found on the basis of scenario that considers H_2O, O_3, CO_2, and $ClONO_2$ as major interfering species have errors exceeding 100 %. The other scenario defined over the spectral interval 935-960 cm^{-1} considers H_2O and CO_2 to be major and NH_3 to be minor absorbers. There are relatively strong signal of COF_2 as a result of

which the two microwindows reported here have retrieval error less than 100 %.

Trichlorofluoromethane (CCl_3F)

CCl_3F is another halocarbon which plays an important role in stratospheric ozone depletion and which is one of powerful greenhouse gases. The profile used is the profile defined for polar atmospheric model. The best microwindow found covers the spectral region 843.1672 – 844.7329 cm^{-1} with a retrieval error of 2.3 % of total column amount of CCl_3F. As the forward simulation is based on cross-section data for all families of Chlorofluorocarbons (CFC), we have only reported the selected microwindows unlike the molecules where line data are provided (see Table 4). The major interfering species considered are H_2O, HNO_3 and OCS. The minor interference comes from NH_3, C_2H_6, CHF_2Cl and ClO. The problem with broad-band absorbers like CFC's is that the background signal is not known accurately. Therefore, for CFC's our results have to be treated with some caution as we have assumed accurate knowledge of the background radiance.

One of the microwindows currently in use by some research groups encompasses a very wide interval from 835-855 cm^{-1} which is nearly a complete spectral region in which CCl_3F has transition and suffers from a number of error sources. Indeed, there are several microwindows in the interval with less than 10 % error. However, there are equally good microwindows outside this spectral interval with even more sampling grid points.

Dichlorofluoromethane (CCl_2F_2)

It is the source of chlorine and fluorine radicals. CCl_2F_2 exhibits wide and strong absorption features in the mid IR located between 860-950 cm^{-1}. The polar profile has been used.

The major interfering species are H_2O and HNO_3 for spectral region in which best microwindows are found. The best microwindows are found in the region between 919-923 cm^{-1} with error less than 2 % of the total column amount. The weak absorbers are NH_3, CO_2, C_2H_6, COF_2 and ClO.

Difluorochloromethane (CHF_2Cl)

Unlike some of the halocarbons, it has low photolysis rate. The mean profile given by

Echle et al (1992) has been slightly changed by a scale factor of 1.4 to account for annual rise in the concentration.

Several microwindows are found for the scenario defined over spectral region 780-830 cm^{-1} which assumes H_2O and CO_2 as major interfering species and C_2H_6, NH_3, C_2H_2, CCl_4, HCN, $ClONO_2$, ClO, COF_2 and HNO_4 as weak species. The microwindow that has been used todate seems to be a good one with small retrieval error.

Water vapor (H_2O)

Atmospheric H_2O plays an important part in the troposphere in most phonemena apart from its effects as main component of the greenhouse gases. A search for optimum microwindow, when uncertainties in pressure, temperature and angle of sight are assumed to be among parameters that contribute to some fraction of the systematic part of the error budget of the retrieval, resulted in extremely very narrow microwindows which consist of only one grid point in the majority of the microwindows that are best in terms of their total retrieval errors. The results are given in the Appendix.

Hydrogen Cyanide (HCN)

It is produced in the atmosphere by both natural biological and anthropogenic means. Owing to small fluctuation in the measurements made, one mean profile had been defined and has been also used in this work. The distribution of HCN is controlled mainly by atmospheric transport. As to the difference spectra, H_2O, CO_2 and O_3 are the major absorber in the spectral region 710-800 cm^{-1} in which HCN has some signal. Weak interference comes from HNO_3, NH_3, C_2H_6, C_2H_2, CHF_2Cl, CCl_4 and COF_2 lines. The result shows that HCN can be retrieved with an accuracy of at most 31 % if the major interfering species are simultaneously fitted during the retrieval and the weaker species are considered as contributor to systematic errors.

Nitric Acid (HNO_3)

HNO_3 plays an important role in the chemistry of the atmosphere because it is a reservoir for the odd nitrogen species that catalytically controls the ozone abundances and it

may act as a sink of NO_y. It is also involved in the heterogeneous and heteromolecular condensation process which is an important precondition for the formation of the polar ozone hole. The tropospheric value of polar profile is reduced by a factor of 0.1 and then used.

HNO_3 is one of the species that can be determined with more accuracy. There are many microwindows with retrieval errors below 10 % under different scenarios over different spectral regions under investigation.

Ammonia (NH_3)

It is primarily produced by biogenic activity on the surface of the earth. It is seen that there is a wide range in the measured vmr in troposphere and stratosphere as a result of which only mean profile is defined and used.

NH_3 has transitions nearly over the complete spectral region investigated. As the major species that have blending effect with NH_3 are not the same over the wide spectral region, we defined nine scenarios of which five are turned out to be useful to retrieve NH_3 with errors below 50 %.

Ozone (O_3)

It is the only atmospheric constituent which effectively absorbs ultraviolet solar radiation from about 250 to 310 nm, protecting plant and animal life from exposure to harmful radiation. Because of current concern in the possible depletion of Ozone layer, extensive measurements have been made and well documented. The winter polar profile has been used.

O_3 is also highly sensitive to the accuracy by which atmospheric and instrumental-parameters are determined so that many PTAOS microwindows are practically single grid point with nearly same retrieval errors. Therefore, from practical point of view it is rather difficult to make selection of best ones on the basis of their retrieval errors. Some of the these microwindows are given in Appendix.

Carbonyl Sulfide (OCS)

The major sources of tropospheric OCS are natural, examples are oceans, soil and conversion of CS_2, whereas anthropogenic sources represent only quite a small fraction.

OCS has signal in the spectral range 828-885 cm^{-1} for which there are different major absorbers. This requires definition of 4 scenarios which are found to be useful as far as the error budget of the determined microwindows is concerned for retrieval under the same condition.

Usually, the species labelled "major interfering species" in Table 2 were treated as joint-fit parameters, however, we also defined scenarios which consider the major interfering parameters in PTAOS as parts to be kept constant instead of jointly fitting in order to validate the decision which parameter to adjust and which to keep constant. Due to obvious reasons (see (41) for estimate of changes that could have occurred as a consequence), the outcome of the optimization has shown that these microwindows besides being quite narrow have large retrieval error. Therefore, they have not been reported here. This confirms that the original of selection joint-fit parameters had been reasonable.

5.1.2 Non-PTAOS Microwindows

These microwindows are determined based on the assumption that in the spectral region under study, absorptions by the trace molecules have weak dependence on these parameters and hence contribution to the systematic portion of the retrieval error due to their a priori uncertainties can be neglected. The motivation behind this case study is as mentioned earlier to allow better comparison to conventionally defined microwindows.

This kind of microwindow optimization has been done only for some selected species as shown in Table 5. The response to the omitted atmospheric and instrumental parameters has shown up in a change of the width of the microwindows in most of the test cases.

Acetylene (C_2H_2)

In this case in which we neglected the the uncertaintities in the three atmospheric model parameters and one instrumental parameter, a completely different set of microwindows are found. One important feature observed is the considerable increase in the width of the microwindows unlike the earlier ones. As a consequence, some of the selected best microwindows include the narrow microwindows selected under PTAOS sensitive scenarios. In addition, they are nearly identical to microwindows that have been widely used such as 766.350-767.175 cm^{-1} given in the atlas of microwindows by, Meier et al. (1997) except a slight difference in both the their borders and width. There is a clear indication that extended spectral regions contain many absorption lines quite sensitive to uncertainties in pressure, temperature and angle of sight.

Chlorine Nitrate ($ClONO_2$)

$ClONO_2$ is another gas for which selection of optimum microwindows has been carried out without the three atmospheric and one instrumental parameters. The result has shown that there are some microwindows (e.g 780.027-781.189 cm^{-1}) which are fairly identical to those reported by Meier et al., (1997).

Chemical Species	microwindow cm^{-1}	Retrieval error (%)	Chemical Species	microwindow cm^{-1}	Retrieval error (%)
C_2H_2	765.9736-767.9422	1.33	H_2O	827.5714-827.8111	0.163
C_2H_2	771.3388-772.3614	2.06	H_2O	838.7251-840.0613	0.108
C_2H_2	761.2612-762.4597	2.96	H_2O	908.6971-910.6938	0.096
C_2H_2	759.0606-760.0908	3.51	H_2O	954.2375-956.2342	0.059
C_2H_2	775.2021-776.1150	3.77	H_2O	952.2332-954.2299	0.071
$ClONO_2$	780.0267-781.1894	3.78	H_2O	939.5852-941.5819	0.089
$ClONO_2$	778.1855-779.1724	9.85	H_2O	943.5836-945.5803	0.090
CO_2	951.8227-951.9502	0.088	H_2O	945.5828-947.5795	0.095
CO_2	948.4057-950.4023	0.089	O_3	994.4460-994.4664	0.653
CO_2	945.0779-947.0746	0.091	O_3	995.4022-995.4252	0.669
CO_2	953.9596-955.9562	0.091	O_3	992.9976-993.0103	0.734
CO_2	970.1394-971.1951	0.091	O_3	994.3465-994.3618	0.739
HNO_3	869.8938-870.5211	0.31	O_3	987.4921-987.5049	0.743
HNO_3	868.8151-869.0880	0.41	O_3	990.2334-990.2410	0.765
HNO_3	870.5899-870.9011	0.41	O_3	994.5454-994.5531	0.776
HNO_3	872.0511-872.4030	0.44	O_3	990.2691-990.2767	0.777
HNO_3	869.1823-869.1798	0.47	O_3	990.2461-990.2538	0.778
H_2O	783.8389-784.8436	0.156	O_3	986.0922-986.1024	0.793
H_2O	778.9735-779.5192	0.157			

Table 5: A list of non-PTAOS microwindows for the gases indicated.

Carbon Dioxide (CO_2)

Similar comparison of PTAOS microwindows with existing microwindows is made but none of the best PTAOS microwindows are identical to existing ones (Meier et al., 1997). Then, the comparison with non-PTAOS microwindows have shown that some non-PTAOS microwindows are found to match the existing ones (e.g 936.100-937.400 cm^{-1}). All the three cases considered so far have pinpointed that microwindows that have been used by many investigators suffer from the same sources of systematic errors. This is also clearly seen in the retrieval errors since the trend is a fall of retrieval errors in the same direction when compared to the non-PTAOS case (see and compare Tables 4 and 5 for $ClONO_2$, Tables 3 and 5 for C_2H_2 and CO_2).

Nitric Acid (HNO_3)

HNO_3 is the only target gas for which there is no significant change in the width of the microwindows found. However, the current microwindows are totally different from the previous ones. This might be due to temperature dependence of major interfering gases as it is evident from the comparison of line parameters of the major interfering gases (Rothman et al., 1996) in the microwindows selected (for instance, OCS absorption line with E"=164 cm^{-1}) in one of the best non-PTAOS microwindows, and E"=324 cm^{-1} in the best PTAOS microwindows).

Water Vapor (H_2O)

A selection of microwindows has also been made for non-PTAOS test case where a dramatic change both in the total retrieval error and the width has been observed. It may be attributed to very high sensitivity of the absorption features of H_2O (for instance, the water vapor continuum) to a priori uncertainities of these parameters.

Ozone (O_3)

There was only a slight change in the width of the microwindows even under non-PTAOS test case. This may be partly attributed to the fact that O_3 has its peak in the stratosphere as a result of which weak sensitivity to change in pressure.

5.2 Validation

We have selected C_2H_2, $ClONO_2$ and HNO_3 as the test target parameters for retrievals using PTAOS and non-PTAOS microwindows. The measurement noise that has been used during selection of microwindows is randomly generated under Gaussian distribution and superimposed on 50 synthetic spectra. In addition, the a priori uncertainties in the fixed parameters are generated using a random distribution of errors. The root mean squared retrieval error of these "Monte Carlo" test runs, carried out by the retrieval algorithm RAT (Clarmann, 1994), are computed and reported in Table 6. We have also given a typical example of simulated reference and best fit spectrum as shown in Fig. 4.

Chemical Species	microwindow cm^{-1}	RMS Test Retrieval error (%)	Expected Retrieval error(%)	Difference (Exp-Test) (%)
$ClONO_2$*	780.0317-780.2306	8.78	8.97	0.19
$ClONO_2$	780.0267-781.1894	3.04	3.78	0.74
C_2H_2*	771.2853-771.6015	2.83	2.94	0.11
C_2H_2	765.9736-767.9422	1.85	1.33	-0.52
HNO_3*	862.5319-863.0776	1.35	0.87	-0.48
HNO_3	872.0511-872.4030	0.34	0.44	0.10

Table 6: A comparison of the test retrieval error with the optimum retrieval error for selected cases. Asterisk denotes PTAOS microwindow.

The root mean squared retrieval error (RMS) has been compared to the value obtained from the optimization by (45). As shown in the last column of the Table 6, there is no considerable difference between the expected retrieval error and error from test runs. For most cases, the predicted retrieval error is well validated by these test retrievals. The observed discrepancy may arise possibly due to many factors. Recall Eqs.(39) and (41) which are basically the same and should lead to identical results. Nevertheless, the way they are implemented have to be taken into account. For instance, if we look at the Levenberg-Marquardt method, it generalizes the method of normal equations, however, it suffers from the same problem with regard to near-degeneracy minimum (Niple, 1980 and Press et al, 1990). Hence, the ultimate decision for whether or not a given solution is the true minimum is usually a subjective one. On the other hand, the most probable profiles used here are not obtained by nonlinear least squares refinement from initial guess but

rather are predefined on the assumption that these are realistic profiles from which the reference spectra were obtained. Therefore, these two difference might have contributed some part to the observed discrepancy.

In addition, the Gaussian distribution of errors in the parameters might have transformed to assymetric distribution of errors in the simulated spectra due to nonlinearity in the Gaussian distribution itself.

The other possible factor might be linked with the fact that the estimates of systematic errors during selection of microwindows have been carried out using difference spectra calculated at an increment of 10 % of vmr which may not be suitable increment for all the parameters thereby introducing nonlinearity.

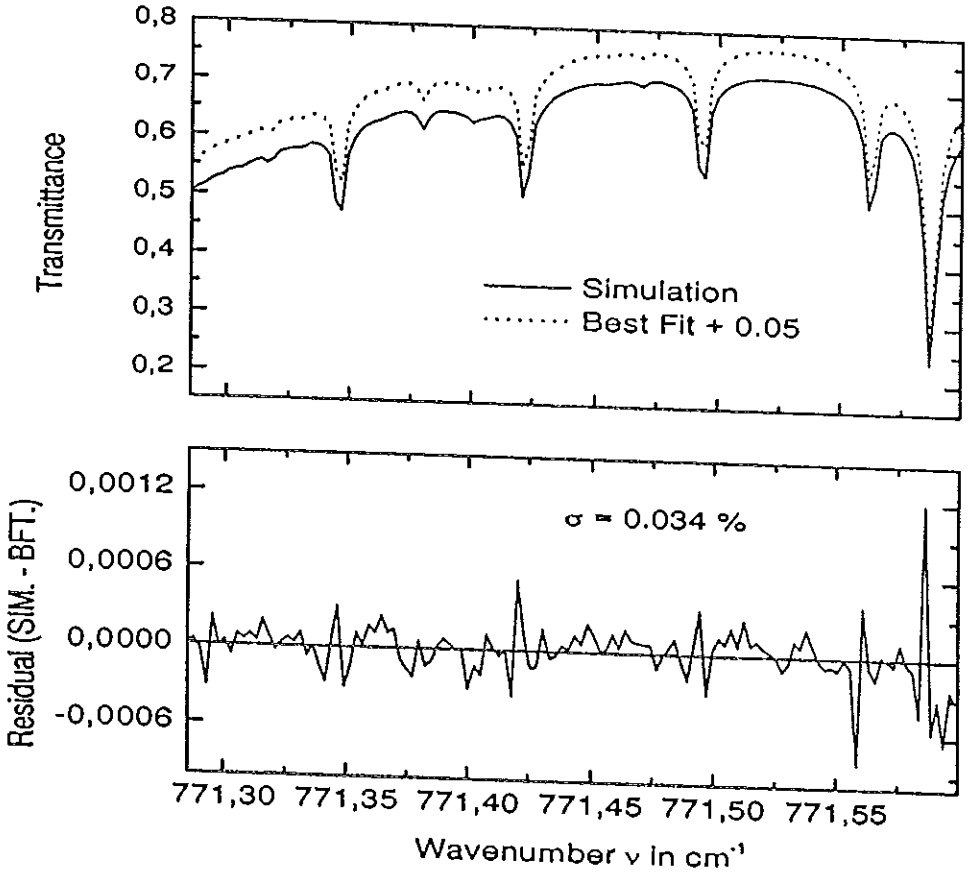

Figure 4: The simulated reference and best fit spectrum for Retrieval of C_2H_2 in the selected PTAOS microwindow.

We have mentioned so far some of the apparent reasons for the observed difference between

expected retrieval errors and those from test retrievals. An important fact underlying the selection of microwindows is not to quantify the errors in the derived parameters but rather to use those values in identifying the most suitable spectral region from the whole spectrum for retrieval of the target gas(es). Nevertheless, as said before, predicted errors are in reasonable and sometimes even excellent agreement with Monte Carlo simulations.

The result of the retrievals using the PTAOS and non-PTAOS microwindows as shown in Table 6 revealed that Monte Carlo retrieval errors in non-PTAOS microwindows are smaller than that of PTAOS in agreement with predicted retrieval errors for all the three species. It indicates that in non-PTAOS case, the total error is underestimated. This can also be observed from test runs undertaken with the three non-PTAOS microwindows but with PTAOS retrieval scenarios of $ClONO_2$, C_2H_2 and HNO_3 since the retrieval errors change to 7.28 %, 17.86 % and 2.64 % respectively. These values differ from both expected errors and non-PTAOS test retrievals quite significantly. Moreover, there is no advantage of using non-PTAOS over PTAOS microwindows as revealed by this results with exception of $ClONO_2$. At first glance it seems suspicious that results for a non-PTAOS microwindows applied to PTAOS conditions yields better results than the " optimum" PTAOS microwindows. The explanation is that the information content of the wide non-PTAOS microwindow is more than that of the narrow PTAOS microwindow. However, it should be compared not to the best PTAOS microwindow alone but to a certain combination of high priority PTAOS microwindows within the spectral region covered by the non-PTAOS microwindows. The combined retrieval error of this microwindow combination is expected to be smaller than the 7.28 %. The microwindows selected by optimization under the two cases may be used jointly in a two step retrieval method used for instance by Reisinger et al. (1995). In a first step the method use a wide microwindow for joint retrievals of target and interfering species. The second step then is a refinement of the target parameter on the basis of a narrow microwindow which is a subset of spectral grid points of the wide microwindow.

6 Conclusion

The theory of radiative transfer has been briefly reviewed in view of both foward and inverse modellings whose applications are sought for ground-based observing system, an example of which is FTIR spectrometer. The forward radiative transfer model is used to simulate reference spectrum and 21 increment spectra corresponding to 17 target species, 3 atmospheric parameters and 1 instrumental parameter based on the realistic atmospheric model developed from independent methods and radiosonde data.

We have also given a short description of error analysis method that can be used for nonlinear models such as radiative transfer models. It has been adopted to microwindow optimization. The result of selection of optimum microwindows proved to be quite successful with regard to encompasing prominent features of the target parameters. However, there are also some exceptions when comparison with existing microwindows are made. Absorption features once assumed to be prominent in terms of strength, less interference from other species and weak sensitivities to changes in certain parameters such as temperatures, pressure etc. are unfortunately found to be contaminated by features of other species which are slightly weaker in strength but highly sensitive to changes in the parameters mentioned. As a result, those features appear in low priority microwindows with regard to associated retrieval errors. Therefore, most of the PTAOS microwindows do not include existing microwindows.

When uncertainties in pressure, temperature and angle of sight are excluded from retrieval scenarios for optimization of microwindows we have noticed dramatic changes both on the type and width of the microwindows. The best non-PTAOS microwindows are fairly identical to the existing ones (Meier et al., 1997). This result has, to certain extent, confirmed that the existing microwindows might have suffered from the same type of systematic error sources.

We have compared retrieval results from selected microwindows in both cases under study to the corresponding optimum retrieval errors claimed. There are only small differences, however, this has no significant implication since the magnitudes of both quantities are

very small compared to the quantity to be derived from the measurement as well as the accuracy by which this quantity used to be determined. The possible explanation for the observed discrepancy are:

1. the transformation of Gaussian distribution of errors in the parameters might have introduced some asymmeteric error distribution in the parameters,

2. the assumed initial guess in the case of retrieval might have been to far away from the real profile due to the nature of nonlinear least squares estimation,

3. contrary to 2, the best estimate is predetermined in the case of microwindow optimization which certainly affects the result as least squares refinement is expected not to give the same best estimate had we started from initial guesses,

4. the 10 % increment for computing the increment spectra might have not satisfied the linearity condition.

There is also a potential error source in case of measured spectra. In the theory of least square analysis, the model is assumed to be exact, but the model (see (25) and steps taken to) is only a good approximation. Although, quantification of the error resulted from model imperfection (Clarmann and Echle, 1997) can also be accounted for during selection of microwindows, this has not been included in this work. The retrieval error arising from model imperfection for the case of simulated spectrum, indeed, does not contribute to the discrepancies observed as in this case the model describes exactly the simulated spectra which is considered as if it is a measured spectrum.

In summary, these microwindows are the first ever reported optimized microwindows which may prove to be useful for the analysis of ground-based FTIR spectra.

References

[1] Adrian, G.P. et al., 1991: Column amounts of trace gases derived from ground-based measurements with MIPAS during CHEOPS III. Geophys. Res. Lett., Vol. 18, No. 4, 783-786.

[2] Adrian, G.P. et al., 1992: Trace Gas Measurement with the Ground-based MIPAS Experiment during the Arctic Winters 1990 to 1992, A.Deepak Publishing.

[3] Bauman, R.P., 1962 : Absorption Spectroscopy, John Wiley & Sons, Inc..

[4] Beer, R., 1992: Remote Sensing by Fourier Transform Spectrometery, John Wiley & Sons. Inc..

[5] Bell, R.J., 1972: Introductory Fourier Transform Spectroscopy, Academic Press, Inc. Ltd, London.

[6] Benner, D.C. et.al, 1995: A Multispectrum Nonlinear Least Squares Fitting Technique, J. Quant. Spectrosc. Radiat. Transfer, Vol. 53, No. 6, 705-721.

[7] Brown, L.R. et al., 1992: Remote Sensing of the Atmosphere by High Resolution Infrared Absorption Spectroscopy. Presented in a book on Spectroscopy of the Earth's Atmosphere and Interstellar Medium by K. Naraharirao et al, Academic Press, 97-151.

[8] Chandrasekhar, S., 1960: Radiative Transfer, Dover Publications, Inc., New York.

[9] Chang,Y.S et al., 1977: Determination of Abundances of Gases from Solar Spectra, J. Quant. Spectrosc. Radiat. Transfer, Vol. 19. 599-605.

[10] Clarmann, T.v., 1993: Retrieval of stratospheric O_3, HNO_3 and $ClONO_2$ profiles from 1992 MIPAS-B, limb emission spectra: Method, results, and error analysis, J. Geophys. Res., Vol. 98, No.D11, 20495-20506.

[11] Clarmann, T.v., 1994: RAT: A Computational Tool for Retrieval of Atmospheric Trace Gas Profiles from Infrared Spectra, KFK Rep. 5423, Kernforschungszentrum Karlsruhe GmbH, Karlsruhe, Germany.

[12] Clarmann, T.v. and Echle, G., 1997: Selection of Optimized Microwindows, submitted to Applied Optics.

[13] Clifford, A.A., 1973: Multivariate Error Analysis. A handbook of error propagation and calculation in many-parameter systems, Applied Science Publishers Ltd, London.

[14] Clough, S.A. et al., 1986: Atmospheric Radiance and Transmittance: FASCOD2, in proceedings of the Sixth Conference on Atmospheric Radiation, Williamsburg, Va..

[15] Echle, G. et al., 1992: Measurement of Atmospheric Parameters with MIPAS, Final Report for ESA contract 9597/91/NL/SF.

[16] Edwards, D.P., 1987: GENLN2: The New Oxford Line-By-Line Atmospheric Transmission/Radiance Model: Description and Users Guide, Hooke Institute for Cooperative Atmospheric Research Clarendon Laboratory.

[17] Goldman, A. et al., 1983: Spectral Least Squares Quantification of Several Atmospheric Gases from High Resolution Infrared Solar Spectra Obtained at the South Pole, J. Quant. Spectrosc. Radiat. Transfer, Vol. 29, No. 3, 189-204.

[18] Goldman, A. et al., 1986: Quantification of HCl from High-Resolution, ground-based infrared Solar spectra in the 3000 cm^{-1} region, J. Quant. Spectrosc. Radiat. Transfer, Vol. 36, No. 4, 385-387.

[19] Goody, R.M and Young, Y.L., 1989: Atmospheric Radiation Theoretical Basis, Oxford University Press, Inc., 2^{nd} ed..

[20] Gunson, M.R. et al., 1990: Measurements of CH_4, N_2O, CO, H_2O, and O_3 in the Middle Atmosphere by the Atmospheric Trace Molecule Spectroscopy Experiment On Spacelab3, J. Geophys. Res., Vol. 95, No.D9, 13867-13882.

[21] Herzberg, G., 1945: Molecular Spectra and Molecular Structure II. Infrared and Raman Spectra of Polyatomic Molecules, Van Nostrand Reinhold, New York.

[22] Hoell, J.M., Harward, C.N. and Williams, B.S., 1980: Remote infrared Heterodyne Radiometer Measurements of Atmospheric Ammonia Profiles, Geophys. Res. Lett., Vol. 7, 313.

[23] Kyle, T.G., 1993: Atmospheric Transmission Emission & Scattering, Pergamon Press.

[24] Lenoble, J., 1985: Radiative Transfer in Scattering and Absorbing Atmospheres: Standard Computational Procedures, A. Deepak Publishing.

[25] Levenberg, A., 1944: A Method for the Solution of certain Non-linear Problems in Least Squares, Quart. Appl. Math. 2, 164-168.

[26] Lin, C.L. et al., 1979: Retrieval of Information from analysis of Absorption Spectrum, Applied Spectroscopy, Vol. 33, No. 5, 487-491.

[27] Liou, K.N., 1980: An Introduction to Atmospheric Radiation, Academic Press, Inc..

[28] Marquardt, D.W., 1963: An algorithm for Least Squares Estimation of Non-linear Parameters, J. Soc. Indust. Appl. Math. 11, No. 2, 431-441.

[29] Mankin, W.G.,1979: Fourier Transform Method for Calculating the Transmittance of Inhomogeneous Atmospheres, Applied Optics, Vol. 18, No. 20, 3426-3433.

[30] Meier, A., Toon, G.C., Rinsland, C.P., and Goldman, A., June 1997: Spectroscopic Atlas of Atmospheric Microwindows in the middle Infrared, IRF preprint 123.

[31] Niple, E.,1980: Nonlinear Least Squares Analysis of Atmospheric Absorption Spectra, Applied Optics, Vol. 19, No. 20, 3481-3490.

[32] Press, W.H., Flannery, B.P., Teukolsky, S.A., and Vetterling, W.T., 1990: Numerical Recipes in C: The Art of Scientific Computing. Cambridge University Press.

[33] Reisinger, A.R. et al., 1995: Southern Hemisphere Midlatitude Ground-based Measurements of $ClONO_2$: Method of Analysis, Seasonal Cycle and Long Term Trend, J. Geophys. Res., Vol. 100, No.D11, 23183-23193.

[34] Rinsland, C.P. et al., 1982: Ground-based spectroscopic measurement of Atmospheric Hydrogen Cyanide, J. Geophys. Res., Vol. 87, No.C13, 11119-11125.

[35] Rodgers, C.D., 1997: Inverse Methods for Atmospheric Sounding: Theory and Practice, (Draft available on Internet: http://www.atm.ox.ac.uk/ rodgers/)

[36] Rothman, L. et al., 1996: The 1996 HITRAN molecular spectroscopic database and HAWKS (HITRAN Atmospheric Workstations), submitted to J. Quant. Spectrosc. Radiat. Transfer.

[37] Sparks, L., 1997: Efficient Line-by-line Calculation of Atmospheric Coefficients to High Numerical Accuracy, J. Quant. Spectrosc. Radiat. Transfer., Vol. 57, No. 5, 631-650.

[38] Toon, G.C. et al., 1989: Ground-based Infrared Measnrements of Tropospheric Source Gases over Antarctica During the 1986 Austral Spring, J. Geophys. Res., Vol.94, No.D9, 11613-11624.

[39] Twomey, S., 1977: Introduction to the Mathematics of Inversion in Remote Sensing and Indirect Measurements, Elsevier Scientific Publishing Company.

[40] Stiller, G.P. et al., 1995: Retrieval of Tropospheric Versus Stratospheric Partitioning of HCl from Ground-based MIPAS FTIR Spectra, J. Quant. Spectrosc. Radiat. Transfer, Vol. 54, No. 5, 899-912.

Appendix: List of Optimized Microwindows

Table A1: Scenarios for Optimized Microwindows

Spectral interval cm^{-1}	Target gas	Major interfering species (Fit parameters)	Minor interfering species (Fixed parameters)
705.0-800.0 scenario 1	C_2H_2	H_2O, O_3, CO_2	C_2H_6,CHF_2Cl, CCl_4, HNO_3, $ClONO_2$, COF_2, HCN
770.0-831.0 scenario 1	C_2H_6	CO_2	H_2O, HNO_3, NH_3, CCl_3F, CCl_2F_2, C_2H_2, OCS, CCl_4, CHF_2Cl, HNO_4, COF_2, $ClONO_2$, HCN, ClO
829.0-860.0 scenario 2	C_2H_6	OCS, CCl_3F	H_2O, HNO_3, NH_3, CCl_2F_2, C_2H_2, CHF_2Cl, CCl_4, CO_2, HCN HNO_4, COF_2, $ClONO_2$, ClO
710.0-800.0 scenario 1	HCN	H_2O, O_3, CO_2	C_2H_2, C_2H_6, CHF_2Cl, COF_2, NH_3, CCl_4, HNO_3
818.5-850.0 scenario 1	ClO	H_2O, OCS	C_2H_6, NH_3, CHF_2Cl, $ClONO_2$, CCl_3F
848.5-885.0 scenario 2	ClO	H_2O, OCS	C_2H_6, NH_3, CCl_2F_2, HNO_3, CCl_3F
785.0-807.0 scenario 1	CCl_4	H_2O, CO_2, NH_3	O_3, C_2H_6, HNO_3, HCN, HNO_4, COF_2, C_2H_2,CHF_2Cl, $ClONO_2$
750.0-820.0 scenario 1	$ClONO_2$	H_2O, O_3, CO_2	C_2H_2, C_2H_6, CHF_2Cl, HCN, NH_3, COF_2, ClO, CCl_4, HNO_3, HNO_4
830.0-860.0 scenario 1	CCl_3F	H_2O, HNO_3, OCS	NH_3, C_2H_6,CHF_2Cl, ClO
888.5-937.0 scenario 1	CCl_2F_2	H_2O,HNO_3	NH_3, CO_2, C_2H_6, COF_2, ClO
780.0-830.0 scenario 1	CHF_2Cl	H_2O, CO_2	C_2H_6, NH_3, C_2H_2, CCl_4, HCN, $ClONO_2$, ClO, COF_2, HNO_4
828.5-840.0 scenario 2	CHF_2Cl	H_2O,OCS, CCl_3F	C_2H_6, NH_3, C_2H_2, CCl_4, HCN, $ClONO_2$, ClO, COF_2, HNO_4

Table A1 (continued)

Spectral interval cm^{-1}	Target gas	Major interfering species (Fit parameters)	Minor interfering species (Fixed parameters)
800.0-805.0 scenario 1	HNO_4	H_2O, CO_2, CCl_4, CHF_2Cl	NH_3, C_2H_6, ClO, $ClONO_2$,COF_2
840.0-860.0 scenario 1	HNO_3	CO_2, CCl_3F, OCS	C_2H_6, NH_3
858.5-870.0 scenario 2	HNO_3	CO_2, H_2O, OCS	C_2H_6, NH_3
868.5-889.0 scenario 3	HNO_3	CO_2, CCl_2F_2, OCS	C_2H_6, NH_3
887.5-920.0 scenario 4	HNO_3	H_2O, CCl_2F_2	C_2H_6, NH_3
700.0-830.0 scenario 1	CO_2	H_2O	HNO_3, NH_3, C_2H_2, CHF_2Cl, CCl_4, HCN, $ClONO_2$, COF_2, ClO, HNO_4, O_3, C_2H_6,
920.0-995.8 scenario 2	CO_2	H_2O	NH_3, CCl_2F_2, O_3, COF_2
700.0-820.0 scenario 1	H_2O	CO_2, O_3	HNO_3, NH_3, C_2H_2, C_2H_6, CHF_2Cl, CCl_4, HCN, $ClONO_2$, COF_2, ClO, HNO_4
818.5-830.0 scenario 2	H_2O		OCS, NH_3, C_2H_2, C_2H_6, CHF_2Cl, CCl_4, HCN, $ClONO_2$, COF_2, ClO, HNO_4
828.5-860.0 scenario 3	H_2O	OCS, CCl_3F	HNO_3, NH_3, C_2H_2, C_2H_6, CHF_2Cl, CCl_4, HCN, $ClONO_2$, COF_2, ClO, HNO_4
895.5-935.0 scenario 4	H_2O	HNO_3, CCl_2F_2	NH_3, C_2H_2, C_2H_6, CHF_2Cl, CCl_4, HCN, $ClONO_2$, COF_2, ClO, HNO_4
933.5-995.8 scenario 5	H_2O	CO_2	O_3,NH_3, C_2H_2, C_2H_6, CHF_2Cl, CCl_4, HCN, $ClONO_2$, COF_2, ClO, HNO_4

Table A1 (continued)

Spectral interval cm^{-1}	Target gas	Major interfering species (Fit parameters)	Minor interfering species (Fixed parameters)
858.5-887.0 scenario 1	NH_3	H_2O, HNO_3, OCS, CCl_2F_2	C_2H_2, C_2H_6, CHF_2Cl, HCN, $ClONO_2$, COF_2, CCl_4, ClO
885.5-920.0 scenario 2	NH_3	H_2O, HNO_3, CCl_2F_2	C_2H_2, C_2H_6, CHF_2Cl, HCN, $ClONO_2$, COF_2, CCl_4, ClO
918.5-930.0 scenario 3	NH_3	H_2O, HNO_3, CO_2	C_2H_2, C_2H_6, CHF_2Cl, HCN, $ClONO_2$, COF_2, CCl_4, ClO
928.5-970.0 scenario 4	NH_3	H_2O, CO_2	C_2H_2, C_2H_6, CHF_2Cl, HCN, $ClONO_2$, COF_2, CCl_4, ClO
968.5-995.8 scenario 5	NH_3	H_2O, O_3, CO_2	C_2H_2, C_2H_6, CHF_2Cl, HCN, $ClONO_2$, COF_2, CCl_4, ClO
700.0-840.0 scenario 1	O_3		H_2O, HNO_3, C_2H_2, C_2H_6, CHF_2Cl, CCl_4, HCN, $ClONO_2$, COF_2, CO_2
960.0-995.5 scenario 2	O_3		H_2O, COF_2, NH_3, CO_2
838.5-860.0 scenario 1	OCS	H_2O, HNO_3, CCl_3F	NH_3, C_2H_6, ClO, CHF_2Cl
858.5-889.0 scenario 2	OCS	H_2O, HNO_3, CCl_2F_2	NH_3, C_2H_6, ClO, CHF_2Cl
750.0-807.0 scenario 1	COF_2	H_2O, O_3, CO_2, $ClONO_2$	NH_3, C_2H_6, CCl_4, CHF_2Cl, HCN, C_2H_2, HNO_3
935.0-960.0 scenario 2	COF_2	H_2O, CO_2	NH_3
958.5-990.0 scenario 3	COF_2	H_2O, O_3, CO_2	NH_3

Table A2: C_2H_2

Gas	Scenario	Spectral interval [cm^{-1}]	Error [%]
C_2H_2	1	771.2853-771.6015	2.94
C_2H_2	1	759.3538-759.7287	4.23
C_2H_2	1	766.4224-766.7412	4.39
C_2H_2	1	761.5494-762.0517	4.70
C_2H_2	1	763.9770-764.5125	5.24
C_2H_2	1	775.8345-776.0997	6.09
C_2H_2	1	754.9041-755.1999	8.34
C_2H_2	1	780.5316-780.7662	8.80
C_2H_2	1	785.2236-785.6163	9.83
C_2H_2	1	766.7437-767.0089	10.57
C_2H_2	1	773.5726-773.7664	13.53
C_2H_2	1	778.1728-778.4533	13.53
C_2H_2	1	780.7687-780.9600	14.32

Table A3: C_2H_6

Gas	Scenario	Spectral interval [cm^{-1}]	Error [%]
C_2H_6	1	819.2380-819.7301	7.58
C_2H_6	1	815.8082-816.9608	10.54
C_2H_6	1	822.3337-822.4178	14.30
C_2H_6	2	838.2636-838.7098	12.91
C_2H_6	2	830.2591-830.3866	13.92

Table A4: HCN

Gas	Scenario	Spectral interval [cm^{-1}]	Error [%]
HCN	1	747.3356-747.6085	30.94
HCN	1	762.0211-762.2761	33.65
HCN	1	750.0565-750.5231	33.96
HCN	1	753.1497-753.3741	39.29
HCN	1	758.9891-759.2263	41.18

Table A5: ClO

Gas	Scenario	Spectral interval [cm^{-1}]	Error [%]
ClO	1	831.3199-831.9651	174.90
ClO	1	829.1141-829.5579	176.90
ClO	1	832.9570-833.4594	181.79
ClO	1	830.3586-830.6136	190.99
ClO	1	834.2091-834.6324	195.42
ClO	2	857.5492-857.7430	134.68
ClO	2	860.7520-860.9127	139.20
ClO	2	856.3456-856.5292	142.97
ClO	2	862.8813-863.0062	148.53
ClO	2	855.3282-855.4251	156.81
ClO	2	858.6789-858.7171	160.94
ClO	2	859.7371-859.7907	162.33
ClO	2	863.8936-863.9727	171.01
ClO	2	861.8383-861.9123	182.35

Table A6: CCl_4

Gas	Scenario	Spectral interval [cm^{-1}]	Error [%]
CCl_4	1	796.1988-796.8005	12.10
CCl_4	1	794.2251-795.3343	13.70
CCl_4	1	797.5987-798.0960	24.60
CCl_4	1	789.7830-790.4868	25.18
CCl_4	1	795.3369-796.0177	32.97
CCl_4	1	801.0565-801.8929	35.31
CCl_4	1	796.8031-797.1881	37.49
CCl_4	1	791.4965-792.2692	37.81
CCl_4	1	792.7843-793.3172	43.27
CCl_4	1	793.8833-794.2225	45.38
CCl_4	1	793.6182-793.8808	45.76
CCl_4	1	797.1907-797.4763	45.89

Table A7: $ClONO_2$

Gas	Scenario	Spectral interval [cm^{-1}]	Error [%]
$ClONO_2$	1	780.0317-780.2306	8.97
$ClONO_2$	1	780.2332-780.3734	13.02
$ClONO_2$	1	806.8195-807.5820	16.80
$ClONO_2$	1	805.2818-805.8378	22.78
$ClONO_2$	1	786.1696-786.6975	24.37
$ClONO_2$	1	782.8775-783.3901	24.62

Table A8: CCl_3F

Gas	Scenario	Spectral interval [cm^{-1}]	Error [%]
CCl_3F	1	843.1672-844.7329	2.31
CCl_3F	1	848.1372-848.9328	2.96
CCl_3F	1	842.2492-843.1647	3.49
CCl_3F	1	850.4475-850.7254	3.72
CCl_3F	1	850.0089-850.4321	3.89
CCl_3F	1	850.7280-850.9549	4.06
CCl_3F	1	841.9713-842.2467	4.26
CCl_3F	1	851.5312-851.7428	4.31
CCl_3F	1	851.1028-851.2813	4.41
CCl_3F	1	841.3388-841.7826	4.42
CCl_3F	1	844.7355-846.1252	4.69
CCl_3F	1	851.3297-851.5210	5.12
CCl_3F	1	851.7454-851.9469	5.18
CCl_3F	1	855.6801-856.8607	5.32
CCl_3F	1	848.9353-849.1036	5.66
CCl_3F	1	856.8632-858.3448	5.96
CCl_3F	1	846.1277-846.8851	6.18
CCl_3F	1	850.9626-851.1003	6.21
CCl_3F	1	849.8023-849.9808	6.40
CCl_3F	1	851.9494-852.0514	6.44
CCl_3F	1	849.1062-849.2515	6.46
CCl_3F	1	849.2541-849.3790	7.04
CCl_3F	1	840.5968-841.2471	7.78
CCl_3F	1	849.6978-849.7768	8.20
CCl_3F	1	847.6884-848.0403	8.45
CCl_3F	1	855.2670-855.6775	8.69

Table A9: CCl_2F_2

Gas	Scenario	Spectral interval [cm^{-1}]	Error [%]
CCl_2F_2	1	919.5779-919.9018	1.73
CCl_2F_2	1	922.9720-923.2627	1.88
CCl_2F_2	1	919.9044-920.6796	1.91
CCl_2F_2	1	929.3853-929.6071	2.30
CCl_2F_2	1	920.9346-921.1947	2.45
CCl_2F_2	1	925.1370-925.3410	2.49
CCl_2F_2	1	919.3229-919.5754	2.85
CCl_2F_2	1	918.8793-919.2260	2.86
CCl_2F_2	1	929.6096-929.7703	3.04
CCl_2F_2	1	926.3125-926.5802	3.09
CCl_2F_2	1	918.5299-918.7390	3.18
CCl_2F_2	1	930.3645-930.6016	3.21
CCl_2F_2	1	921.5109-921.7837	3.22
CCl_2F_2	1	930.0584-930.2497	3.23
CCl_2F_2	1	922.4697-922.6864	3.24
CCl_2F_2	1	917.4691-918.0990	3.24
CCl_2F_2	1	928.2582-928.4902	3.26
CCl_2F_2	1	928.4928-928.6177	3.30
CCl_2F_2	1	929.2909-929.3725	3.32
CCl_2F_2	1	926.5828-926.6848	3.36
CCl_2F_2	1	922.6889-922.8573	3.36
CCl_2F_2	1	914.9676-915.5107	3.46
CCl_2F_2	1	925.9733-926.3100	3.48
CCl_2F_2	1	924.1119-924.5352	3.50
CCl_2F_2	1	911.2981-912.3818	3.52
CCl_2F_2	1	927.4320-927.6232	3.53
CCl_2F_2	1	921.7862-921.8781	3.56
CCl_2F_2	1	922.2274-922.3549	3.57
CCl_2F_2	1	925.6826-925.9249	3.62
CCl_2F_2	1	929.1430-929.1940	3.75
CCl_2F_2	1	926.6975-926.8047	3.77
CCl_2F_2	1	922.8598-922.9695	3.82
CCl_2F_2	1	926.8072-926.9245	3.88
CCl_2F_2	1	916.7602-917.1759	3.97
CCl_2F_2	1	928.8370-928.8957	3.99
CCl_2F_2	1	927.7788-928.0006	4.01
CCl_2F_2	1	930.7164-930.8209	4.10
CCl_2F_2	1	927.6258-927.7278	4.16
CCl_2F_2	1	928.0669-928.2556	4.22
CCl_2F_2	1	929.8545-929.9463	4.33

Table A10: CHF_2Cl

Gas	Scenario	Spectral interval [cm^{-1}]	Error [%]
CHF_2Cl	1	828.8949-829.5502	1.66
CHF_2Cl	1	820.6456-820.9592	3.75
CHF_2Cl	1	809.2114-809.3568	3.84
CHF_2Cl	1	808.7703-809.2088	4.43
CHF_2Cl	1	804.3026-804.5729	4.49
CHF_2Cl	1	817.8737-818.3863	5.71
CHF_2Cl	1	817.1955-817.6187	6.29
CHF_2Cl	1	819.1513-819.6384	6.56
CHF_2Cl	1	815.7853-816.0938	7.01
CHF_2Cl	1	800.9724-801.3472	7.04
CHF_2Cl	1	819.8041-820.2147	7.06
CHF_2Cl	1	801.7654-802.0816	7.82
CHF_2Cl	1	800.1513-800.6128	7.87
CHF_2Cl	1	820.9669-821.7038	8.15
CHF_2Cl	1	799.4220-799.8147	8.21
CHF_2Cl	1	816.1576-816.4126	8.35
CHF_2Cl	1	811.0091-811.7767	8.66
CHF_2Cl	1	814.9897-815.2779	8.83
CHF_2Cl	1	818.7433-819.1411	9.01
CHF_2Cl	1	817.6213-817.8661	9.10
CHF_2Cl	1	816.7467-817.0297	9.56
CHF_2Cl	1	812.6233-813.2328	9.74
CHF_2Cl	2	831.3174-832.5209	6.95

Table A11: HNO_4

Gas	Scenario	Spectral interval [cm^{-1}]	Error [%]
HNO_4	1	802.4029-802.9078	706.85

Table A12: HNO_3

Gas	Scenario	Spectral interval [cm^{-1}]	Error [%]
HNO_3	1	857.0545-858.4264	1.20
HNO_3	2	862.5319-863.0776	0.87
HNO_3	2	863.0827-863.5621	0.93
HNO_3	2	861.7057-862.2463	1.03
HNO_3	2	861.2288-861.6980	1.10
HNO_3	2	860.2496-860.7749	1.12
HNO_3	2	863.5647-863.9191	1.18
HNO_3	2	864.2277-864.5591	1.22
HNO_3	2	860.7800-861.2187	1.28
HNO_3	2	866.0738-866.2957	1.39
HNO_3	2	862.2488-862.5294	1.40
HNO_3	2	863.9216-864.0619	1.43
HNO_3	2	865.6990-865.8443	1.46
HNO_3	2	866.4869-866.7394	1.51
HNO_3	3	878.1915-878.4159	1.30
HNO_3	3	879.7980-880.4023	1.34
HNO_3	3	885.0994-885.3009	1.38
HNO_3	3	877.4443-877.9237	1.41
HNO_3	3	879.3543-879.7929	1.43
HNO_3	3	880.4049-880.7364	1.45
HNO_3	3	884.2656-884.5996	1.48
HNO_3	4	895.5544-895.7865	1.20
HNO_3	4	893.2951-893.5858	1.23
HNO_3	4	893.8459-894.2029	1.29
HNO_3	4	895.2713-895.5519	1.31
HNO_3	4	909.3270-909.7656	1.32
HNO_3	4	911.4741-912.1014	1.32
HNO_3	4	894.5727-894.9093	1.33
HNO_3	4	910.8315-911.3415	1.34
HNO_3	4	894.9118-895.2637	1.34
HNO_3	4	895.8094-896.0440	1.36
HNO_3	4	910.4235-910.8289	1.37
HNO_3	4	892.4383-892.6959	1.37
HNO_3	4	896.9263-897.5281	1.39
HNO_3	4	890.7120-890.9440	1.40
HNO_3	4	912.3793-913.0704	1.41
HNO_3	4	892.6984-892.8310	1.41
HNO_3	4	898.5379-899.2570	1.49
HNO_3	4	909.7681-909.9950	1.51
HNO_3	4	889.6333-889.7685	1.52

Table A13: CO_2

Gas	Scenario	Spectral interval [cm^{-1}]	Error [%]
CO_2	1	805.9933-806.2228	1.00
CO_2	1	769.5615-770.2245	1.20
CO_2	1	806.3809-806.6742	1.47
CO_2	1	802.9384-803.0914	1.51
CO_2	1	767.2563-767.5189	1.54
CO_2	1	799.1210-799.9728	1.83
CO_2	1	796.9153-797.6599	1.95
CO_2	1	807.8931-807.9593	2.03
CO_2	1	827.8876-828.5506	2.04
CO_2	1	768.2380-769.0897	2.12
CO_2	1	803.8130-804.6137	2.14
CO_2	1	813.7938-814.0003	2.17
CO_2	1	752.3745-752.4714	2.18
CO_2	1	751.8058-751.9511	2.19
CO_2	1	826.5259-827.0385	2.22
CO_2	1	753.6163-754.0090	2.35
CO_2	1	814.0972-814.4287	2.36
CO_2	1	800.0875-800.1742	2.38
CO_2	2	944.0834-944.1345	1.14
CO_2	2	968.9893-969.0607	1.20
CO_2	2	969.1958-969.2443	1.20
CO_2	2	938.5933-938.6418	1.39
CO_2	2	961.7550-961.9360	1.39
CO_2	2	955.6783-956.1245	1.41
CO_2	2	947.8651-948.3419	1.68
CO_2	2	950.8792-951.0296	1.73
CO_2	2	947.5566-947.6279	1.75
CO_2	2	949.6093-949.6985	1.80
CO_2	2	944.2568-944.3130	1.84
CO_2	2	969.2979-969.4049	1.88
CO_2	2	953.0390-953.2940	1.96
CO_2	2	959.4395-959.6971	1.96
CO_2	2	956.4331-957.5271	1.99
CO_2	2	970.8279-971.1746	2.06
CO_2	2	954.1101-954.3854	2.07
CO_2	2	952.6897-952.7713	2.18
CO_2	2	974.0026-974.5075	2.23
CO_2	2	970.3179-970.4071	2.25
CO_2	2	942.4438-942.4769	2.39
CO_2	2	960.4723-961.6555	2.42

Table A14: H_2O

Gas	Scenario	Spectral interval [cm^{-1}]	Error [%]
H_2O	1	784.8589-785.0145	1.01
H_2O	1	760.5447-760.6772	1.05
H_2O	1	787.4319-787.8194	1.18
H_2O	1	815.3799-815.5252	1.26
H_2O	1	753.5118-753.7821	1.26
H_2O	1	783.7063-783.8007	1.38
H_2O	1	803.9559-804.3638	1.50
H_2O	2	825.2407-825.2560	1.14
H_2O	2	825.9955-827.1864	1.23
H_2O	2	825.1387-825.2127	1.24
H_2O	2	827.3496-827.4159	1.26
H_2O	2	825.2917-825.3351	1.39
H_2O	2	825.2586-825.2636	1.40
H_2O	2	827.4184-827.4312	1.44
H_2O	2	827.4337-827.4745	1.52
H_2O	2	827.8646-829.0326	1.53
H_2O	2	825.3376-825.3504	1.57
H_2O	3	841.9457-842.2058	0.73
H_2O	3	852.5155-852.6124	1.43
H_2O	4	924.8743-924.9126	1.21
H_2O	5	946.2254-946.7201	0.84
H_2O	5	973.8827-973.9414	0.88
H_2O	5	959.4625-959.6486	0.98
H_2O	5	972.1691-972.3629	0.98
H_2O	5	954.1049-954.4007	1.10
H_2O	5	948.6530-949.0049	1.11
H_2O	5	940.1947-940.4089	1.16
H_2O	5	959.9368-960.5156	1.24
H_2O	5	958.5445-959.3681	1.28
H_2O	5	955.2881-955.3162	1.29
H_2O	5	955.6732-957.0731	1.31
H_2O	5	937.0097-937.3616	1.32
H_2O	5	948.1711-948.2017	1.36
H_2O	5	947.4469-947.6203	1.39
H_2O	5	952.6693-952.8019	1.39
H_2O	5	952.9778-953.2328	1.46
H_2O	5	940.5721-940.9877	1.46
H_2O	5	944.2721-944.8510	1.47
H_2O	5	978.6971-978.8909	1.51
H_2O	5	938.7539-938.8508	1.54

Table A15: NH_3

Gas	Scenario	Spectral interval [cm^{-1}]	Error [%]
NH_3	1	867.7084-868.3536	1.42
NH_3	1	872.2500-872.9308	3.03
NH_3	1	866.7496-867.6982	3.49
NH_3	2	887.5907-888.3302	1.73
NH_3	2	891.8212-892.3669	1.83
NH_3	2	908.1973-908.3962	2.28
NH_3	2	908.0111-908.1947	2.31
NH_3	3	927.0290-927.3452	1.16
NH_3	3	929.4923-929.9004	1.49
NH_3	3	928.4264-928.7477	2.38
NH_3	3	923.2652-924.5632	2.73
NH_3	3	928.7503-928.9645	2.98
NH_3	3	925.2899-925.6342	3.59
NH_3	3	927.8195-928.3805	3.67
NH_3	3	929.0231-929.2603	3.81
NH_3	3	927.3478-927.8170	4.51
NH_3	4	964.9960-965.4014	0.91
NH_3	4	930.4970-930.8438	0.92
NH_3	4	967.0589-967.3955	1.43
NH_3	4	967.3981-967.6174	1.55
NH_3	4	931.5119-931.8383	1.74
NH_3	4	951.2974-951.8125	1.79
NH_3	4	929.5586-929.8978	2.08
NH_3	4	929.9004-930.0839	2.20
NH_3	4	963.9837-964,5421	2.24
NH_3	4	961.8671-962.5811	2.31
NH_3	4	928.5361-928.7452	2.46
NH_3	4	965.4040-965.7865	2.73
NH_3	4	928.7477-928.9645	2.87
NH_3	4	933.6386-934.7759	3.20
NH_3	4	930.0865-930.4945	3.22
NH_3	4	963.0911-963.4201	3.34
NH_3	4	966.7631-966.8524	3.38
NH_3	4	951.8150-952.3276	3.62
NH_3	4	931.8409-932.1367	3.69
NH_3	4	966.8830-967.0436	3.77
NH_3	4	931.2799-931.5094	4.29
NH_3	4	963.4226-963.9811	4.59
NH_3	4	932.2897-932.9144	5.43
NH_3	5	992.5156-992.7094	1.43

Table A16: O_3

Gas	Scenario	Spectral interval [cm^{-1}]	Error [%]
O_3	1	771.7646-771.7672	2.72
O_3	1	765.4305-765.4330	2.77
O_3	1	767.0752-767.0778	2.79
O_3	1	763.9846-763.9897	2.80
O_3	1	778.0376-778.0402	2.83
O_3	1	773.3099-773.3125	2.85
O_3	2	992.1739-992.1765	1.81
O_3	2	994.1247-994.1272	1.93
O_3	2	993.2015-993.2041	1.94
O_3	2	995.1498-995.1523	1.99
O_3	2	993.4999-993.5025	2.14
O_3	2	994.1629-994.1655	2.23
O_3	2	993.6376-993.6402	2.27
O_3	2	993.4311-993.4336	2.30
O_3	2	991.6537-991.6614	2.32
O_3	2	992.9925-992.9950	2.40
O_3	2	995.4966-995.4991	2.44
O_3	2	991.1641-991.1667	2.45
O_3	2	994.3465-994.3542	2.51
O_3	2	991.4089-991.4115	2.51
O_3	2	991.7991-991.8067	2.55
O_3	2	989.1802-989.1828	2.56
O_3	2	989.3434-989.3460	2.56
O_3	2	995.1549-995.1574	2.58
O_3	2	992.4672-992.4697	2.60
O_3	2	994.7673-994.7698	2.62
O_3	2	989.4097-989.4148	2.62
O_3	2	991.2126-991.2151	2.62
O_3	2	991.4701-991.4727	2.63
O_3	2	994.3644-994.3669	2.63
O_3	2	992.9976-993.0001	2.65
O_3	2	990.7638-990.7663	2.66
O_3	2	994.5352-994.5403	2.66
O_3	2	994.4689-994.4740	2.70
O_3	2	992.9542-992.9695	2.72
O_3	2	994.1298-994.1323	2.76
O_3	2	992.1790-992.1816	2.78
O_3	2	994.5531-994.5633	2.78
O_3	2	993.2067-993.2092	2.80
O_3	2	994.4766-994.4791	2.90

Table A17: OCS

Gas	Scenario	Spectral interval [cm^{-1}]	Error [%]
OCS	1	842.5476-844.5340	9.34
OCS	1	855.6265-857.4752	9.91
OCS	1	848.0530-848.9557	10.33
OCS	1	845.6560-846.5562	10.84
OCS	1	844.5366-845.6381	10.91
OCS	1	849.9732-850.4321	12.42
OCS	1	850.4347-850.8172	12.53
OCS	1	846.5587-847.0024	15.17
OCS	1	850.8197-851.2558	15.32
OCS	1	851.5032-851.9188	15.92
OCS	1	853.5075-853.7421	16.97
OCS	1	847.0050-847.3339	20.06
OCS	1	849.5193-849.9324	20.20
OCS	1	853.7446-854.0914	21.18
OCS	1	847.5838-847.8872	23.44
OCS	1	855.2083-855.5780	23.61
OCS	1	851.3757-851.5006	24.31
OCS	1	847.8898-848.0504	25.11
OCS	1	853.1300-853.2499	25.89
OCS	1	854.7978-855.2057	26.38
OCS	1	841.0201-841.6550	27.98
OCS	1	842.0580-842.5450	29.02
OCS	1	849.1801-849.3968	30.18
OCS	2	870.1028-870.7352	9.52
OCS	2	868.3688-868.9477	10.66
OCS	2	866.6986-867.1499	11.81
OCS	2	868.9502-869.2767	12.16
OCS	2	873.3184-874.2262	13.12
OCS	2	869.7305-870.1003	13.29
OCS	2	867.4407-867.6242	13.64
OCS	2	868.0960-868.3663	13.87
OCS	2	874.2287-875.2742	16.00
OCS	2	872.7778-873.3158	18.82
OCS	2	871.8827-872.3265	22.20
OCS	2	869.2792-869.7280	22.42
OCS	2	870.7455-870.9469	25.22
OCS	2	872.6477-872.7753	27.98
OCS	2	867.1525-867.2800	28.18
OCS	2	875.2768-875.8990	28.77
OCS	2	871.4212-871.6762	30.72

Table A18: COF_2

Gas	Scenario	Spectral interval [cm^{-1}]	Error [%]
COF_2	1	773.5598-773.9933	96.02
COF_2	1	773.9959-774.1055	101.02
COF_2	2	956.5938-957.6316	71.97
COF_2	2	957.9070-958.7663	87.07
COF_2	2	951.9936-952.7356	101.90
COF_2	2	950.3080-950.8486	146.45
COF_2	2	953.6255-954.0055	148.94
COF_2	3	972.4190-973.0362	103.37
COF_2	3	968.1707-968.8949	112.84
COF_2	3	969.7722-970.1266	129.91
COF_2	3	962.4358-963.2492	137.45
COF_2	3	969.4356-969.7543	139.94